The Astrophysical Journal, 929:186 (21pp), 2022 April 20 https://doi.org/10.3847/1538-4357/ac5d4e

The ESO-VLT MIKiS Survey Reloaded: Velocity Dispersion Profile and Rotation Curve of NGC 1904*

Silvia Leanza[1,2], Cristina Pallanca[1,2], Francesco R. Ferraro[1,2], Barbara Lanzoni[1,2], Emanuele Dalessandro[2], Livia Origlia[2], Alessio Mucciarelli[1,2], Elena Valenti[3,4], Maria Tiongco[5], Anna Lisa Varri[6,7], and Enrico Vesperini[8]
[1] Dipartimento di Fisica e Astronomia, Università di Bologna, Via Gobetti 93/2 I-40129 Bologna, Italy; silvia.leanza2@unibo.it
[2] INAF-Osservatorio di Astrofisica e Scienze dello Spazio di Bologna, Via Gobetti 93/3 I-40129 Bologna, Italy
[3] European Southern Observatory, Karl-Schwarzschild-Strasse 2, D-85748 Garching bei Munchen, Germany
[4] Excellence Cluster ORIGINS, Boltzmann-Straße 2, D-85748 Garching bei München, Germany
[5] University of Colorado, JILA and Department of Astrophysical and Planetary Sciences, 440 UCB, Boulder, CO 80309, USA
[6] Institute for Astronomy, University of Edinburgh, Royal Observatory, Blackford Hill, Edinburgh EH9 3HJ, UK
[7] School of Mathematics, University of Edinburgh, Kings Buildings, Edinburgh EH9 3FD, UK
[8] Department of Astronomy, Indiana University, Bloomington, IN 47401, USA
Received 2021 October 25; revised 2022 March 3; accepted 2022 March 10; published 2022 April 27

Abstract

We present an investigation of the internal kinematic properties of M79 (NGC 1904). Our study is based on radial velocity measurements obtained from the ESO-VLT Multi-Instrument Kinematic Survey (MIKiS) of Galactic globular clusters for more than 1700 individual stars distributed between ∼0.″3 and 770″ (∼14 three-dimensional half-mass radii) from the center. Our analysis reveals the presence of ordered line-of-sight rotation with a rotation axis almost aligned along the east–west direction and a velocity peak of 1.5 km s^{-1} at ∼70″ from the rotation axis. The velocity dispersion profile is well described by the same King model that best fits the projected density distribution, with a constant central plateau at $\sigma_0 \sim 6$ km s^{-1}. To investigate the cluster rotation in the plane of the sky, we have analyzed the proper motions provided by the Gaia EDR3, finding a signature of rotation with a maximum amplitude of ∼2.0 km s^{-1} at ∼80″ from the cluster center. Analyzing the three-dimensional velocity distribution for a subsample of 130 stars, we confirm the presence of systemic rotation and find a rotation axis inclination angle of 37° with respect to the line of sight. As a final result, the comparison of the observed rotation curves with the results of a representative *N*-body simulation of a rotating star cluster shows that the present-day kinematic properties of NGC 1904 are consistent with those of a dynamically old system that has lost a significant fraction of its initial angular momentum.

Unified Astronomy Thesaurus concepts: Globular star clusters (656); Stellar kinematics (1608); Spectroscopy (1558)

1. Introduction

Galactic globular clusters (GGCs) are the most populous and oldest stellar systems where stars can be individually observed. Moreover, they are collisional systems, where the frequent gravitational interactions among stars can make the characteristic timescale for dynamical evolution significantly shorter than their age, depending on intrinsic properties at formation (e.g., total mass, central mass density, binary content, etc.) and external effects in the environment in which they are embedded (e.g., Galactic tides, disk shocks). In fact, in spite of their similar chronological ages (∼12 Gyr; Forbes & Bridges 2010), GGCs show different stages of internal dynamical evolution (see Ferraro et al. 2020 and references therein) and therefore are ideal laboratories where the complex interplay between stellar population properties and dynamical evolutionary effects can be empirically investigated. The innermost core regions of GGCs are expected to offer the ideal environment for the occurrence of stellar interactions able to generate exotic objects, like interacting binaries, blue stragglers, millisecond pulsars (Bailyn 1995; ; Ferraro et al. 1997, 2003, 2018a; Pooley et al. 2003; Ransom et al. 2005), and even the long-sought class of intermediate-mass black holes (IMBHs; e.g., Giersz et al. 2015). Indeed, the extrapolation of the "Magorrian relation" (Magorrian et al. 1998) down to the IMBH mass scale naturally leads to the mass regime of GGCs for the hosting stellar system. In addition, numerical simulations (e.g., Portegies Zwart et al. 2004; Freitag et al. 2007; Giersz et al. 2015) confirm that GGCs are ideal habitats for the formation of IMBHs. The accurate characterization of GGCs in terms of their structural properties, internal kinematics, and dynamical status is a crucial step for the proper understanding of how dynamical processes affect the evolutionary history of these systems and impact the formation of stellar exotica.

Our group is addressing this problem by combining a variety of complementary perspectives: (i) by constructing a new generation of high-quality star density profiles derived from star counts instead of surface brightness (see Lanzoni et al. 2007a, 2010, 2019; Miocchi et al. 2013; Pallanca et al. 2021); (ii) by investigating the population of stellar exotica (Ferraro et al. 2001, 2003, 2015, 2016; Pallanca et al. 2010, 2013, 2014, 2017; Cadelano et al. 2017, 2018, 2020) and their connection with the dynamical evolution of the parent cluster (see Ferraro et al. 2009, 2012, 2018a, 2019; Lanzoni et al. 2016); (iii) by characterizing the three-dimensional (3D) global

* Based on observations collected at the European Southern Observatory, Cerro Paranal (Chile), under proposal 193.D-0232 (PI: Ferraro) and 0104.D-0636 (PI: Ferraro).

velocity space through the analysis of the velocity dispersion profile and rotation curve from resolved star spectroscopy (Lanzoni et al. 2013, 2018a, 2018b; Ferraro et al. 2018b) and proper motions (PMs; see Raso et al. 2020). The determination of GGC internal kinematics from resolved star velocities is particularly relevant and challenging. In this context we promoted the ESO-VLT Multi-Instrument Kinematic Survey (hereafter the MIKiS survey; Ferraro et al. 2018b, 2018c), a project specifically designed to characterize the kinematical properties of a sample of GGCs in different dynamical evolutionary stages from the radial velocities (RVs) of hundreds of individual stars distributed over the entire radial range of each stellar system. To this end, the survey fully exploits the spectroscopic capabilities of different instruments currently available at the ESO Very Large Telescope (VLT): originally designed to use the adaptive optics (AO) assisted integral-field spectrograph SINFONI, the multiobject integral-field spectrograph KMOS, and the multiobject fiber-fed spectrograph FLAMES/GIRAFFE, it has been recently complemented with individual projects and an ongoing large program (PI: Ferraro) fully exploiting the remarkable performances of the AO-assisted integral-field spectrograph MUSE.

In this paper, we present the velocity dispersion profile and rotation curve of NGC 1904, a well-known metal-intermediate and low-extinction GGC, with $[\mathrm{Fe/H}] = -1.6$ dex, $E(B-V) = 0.01$ (Harris 1996; Ferraro et al. 1999), and a blue extended horizontal branch (HB; Ferraro et al. 1992; Lanzoni et al. 2007b; Dalessandro et al. 2013). This cluster is particularly intriguing since it was indicated as the possible host of an IMBH of $\sim$3000 $M_{\odot}$ on the basis of the shape of the velocity dispersion profile obtained from integrated-light spectra in the innermost regions of the system (Lützgendorf et al. 2013). In Ferraro et al. (2018b) we presented the line-of-sight kinematics of the external region of the system as obtained from individual RV measurements. Here we complement those data with recent MUSE observations of the innermost $\sim$15″ in the highest available spatial resolution configuration, and with archive MUSE data at lower spatial resolution extending to radial distances of $\sim$67″ from the center.

The paper is organized as follows. Section 2 provides the description of the observations and the adopted data reduction procedures. In Section 3 we discuss the selection of the samples, the determination of the stellar RVs, and the homogenization of the different data sets. The details on the kinematic analysis of the line-of-sight velocities and the derived results are presented in Section 4, together with the results obtained from the analysis of the PMs from Gaia EDR3. The conclusions are then presented in Section 5.

2. Observations and Data Reduction

As discussed above, to construct the velocity dispersion profile of NGC 1904, we complemented the catalog presented in Ferraro et al. (2018b) with a new set of spectroscopic data at high spatial resolution. To acquire spectra of individual stars in the innermost regions of NGC 1904, we took advantage of the superb spatial resolution capabilities of the AO-assisted integral-field spectrograph MUSE in the Narrow Field Mode (NFM) configuration (Bacon et al. 2010). MUSE is mounted on the Yepun, the VLT-UT4 telescope at the ESO Paranal Observatory, and it is equipped with the Adaptive Optics Facility (AOF) of the VLT and the GALACSI-AO module. It has a modular structure composed of 24 identical integral field units (IFUs), and, in the nominal mode,[9] it samples the wavelength range 4800–9300 Å with a spectral resolution $R \sim 3000$ at $\lambda \sim 8700$ Å.

Table 1
MUSE/NFM Data Set

Name	R.A.	Decl.	Date	N_{exp}
C	81.045674	−24.52522	2019-11-05	3
S	81.044944	−24.52612	2019-12-03	3
SE	81.046915	−24.52657	2019-12-04	3
			2019-12-06	3
E	81.049125	−24.52575	2019-12-03	2
W	81.043994	−24.52513	2019-12-04	3
N1	81.046829	−24.52267	2019-12-06	3
N2	81.046788	−24.52191	2019-11-02	2

Note. Name, coordinates (in degree), observation date, and number of exposures (N_{exp}) for each NFM pointing analyzed in this paper.

The NFM data set acquired in NGC 1904 consists of a mosaic of seven MUSE/NFM pointings covering the innermost $\sim$15″ from the cluster center (Lanzoni et al. 2007b), with each pointing having a field of view of 7.″5 × 7.″5 and spatial sampling of 0.″025 pixel^{-1}. The observations have been collected on 2019 November 1–5 and December 2–6 (ESO proposal ID: 0104.D-0636(A); PI: Ferraro; see Table 1). In general, for each pointing three exposures were acquired following a small dithering pattern (smaller than 1.″0). A 90° rotation of the detector has been set between consecutive exposures, in order to correct for possible systematic effects of individual spectrographs, to improve the flat-fielding quality and, hence, to reach a homogeneous image quality across the entire field of view. A series of 835 s long exposures were secured under good seeing conditions: the average DIMM seeing during the observations was always better than $\sim$0.″7.

The NFM data set has been complemented with archive observations (ESO program ID: 098.D-0148(A); PI: Dreizler) acquired with MUSE in the Wide Field Mode (WFM) configuration, providing velocity measures at intermediate distances from the cluster center and allowing a proper overlap with the data presented in Ferraro et al. (2018b). A mosaic of four WFM pointings has been included in the analysis, each pointing having an exposure time of 120 s and providing a 1′ × 1′ field of view, with a spatial sampling of 0.″2 pixel^{-1}. This data set covers a cluster region up to $\sim$67″ from the center, including the area sampled by the high-resolution NFM observations. The wavelength range, the spectral resolution, and the adopted strategy for the acquisition of the images are the same as previously described for NFM observations.

The MUSE data reduction (for both NFM and WFM images) was performed with the dedicated ESO pipeline (Weilbacher et al. 2020). It consists of two main steps. The first one performs the basic reduction of individual IFUs, including bias subtraction, flat-fielding, and wavelength calibration. The second step transforms preprocessed data into physical quantities, by performing the flux calibration, sky subtraction, and astrometric calibration for each IFU and applying the heliocentric velocity correction to all data. Then, the data from

[9] MUSE provides two instrument modes for the wavelength coverage: nominal and extended mode, which correspond to 4800–9300 Å and 4650–9300 Å, respectively.

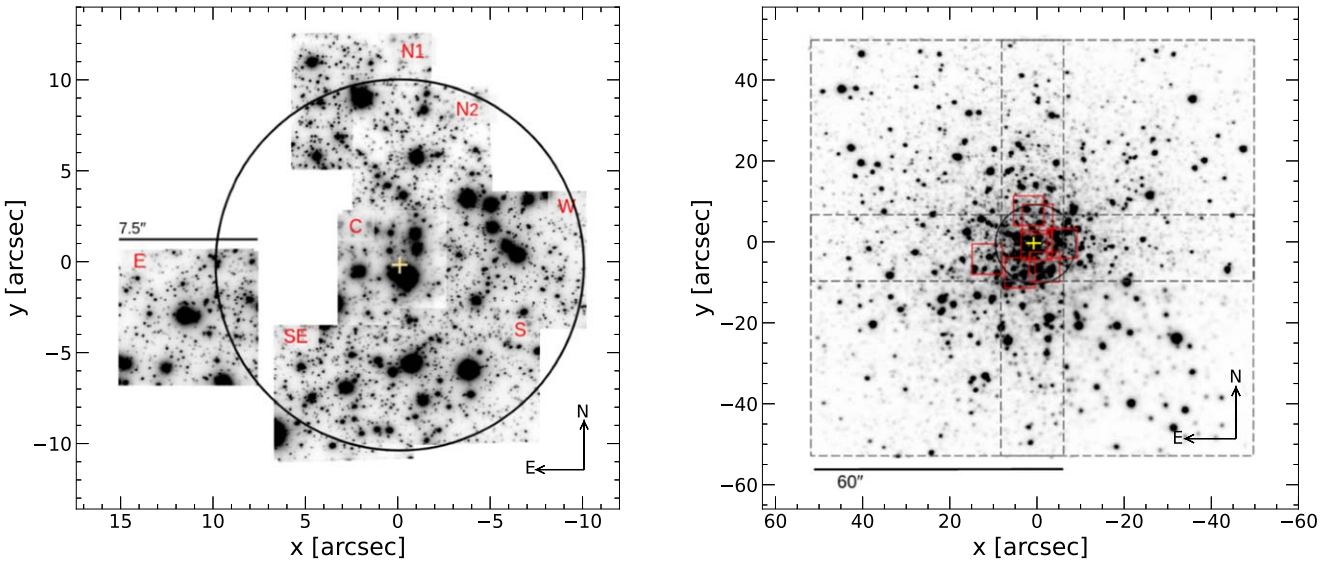

Figure 1. Left: reconstructed *I*-band images of the seven MUSE/NFM pointings. The *x*- and *y*-axes represent the projected positions of the stars with respect to the cluster center (yellow cross, from Lanzoni et al. 2007b). The circle is centered on the center and has a radius of 10″. Right: reconstructed *I*-band image of the four MUSE/WFM pointings (each sampling 60″ × 60″ on the sky; dashed squares), with the location of the seven NFM pointings overplotted in red. The yellow cross and the circle are as in the left panel.

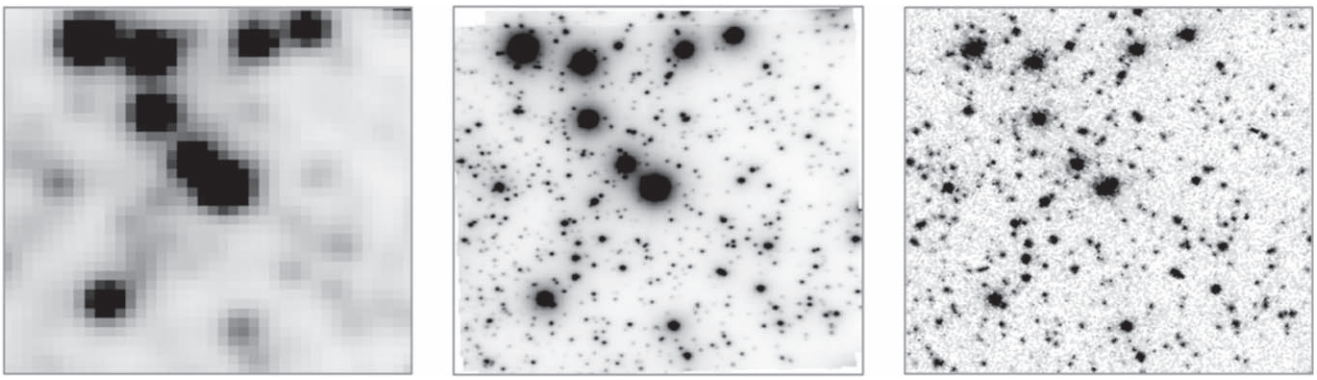

Figure 2. Reconstructed MUSE/NFM image of the W pointing (middle panel), compared with that obtained with the Planetary Camera of the HST/WFPC2 (right panel) and the MUSE/WFM observations (left panel). In all cases the field of view samples an area of ∼8″ × 8″ on the sky.

all 24 IFUs are combined into a single 3D datacube. Finally, the pipeline combines the data cubes of each individual exposure into a single final datacube for every pointing, taking into account possible offsets and rotations among different exposures. Figure 1 (left panel) shows the reconstructed datacube image of the NFM observations for the seven available pointings named according to their position with respect to the cluster center: Center (C), South (S), East (E), West (W), North (N1), North (N2), Southeast (SE). Note that only two exposures were acquired in fields N2 and E because of technical problems. The reconstructed image of the four WFM pointings is shown in the right panel of the same figure.

Indeed, already from a first visual inspection, the NFM observations immediately appear of superb quality, well comparable to the quality of Hubble Space Telescope (HST) images. This can be even better appreciated in Figure 2, where the reconstructed NFM image of the W pointing (middle panel) is compared with an image of the same region as seen from the Planetary Camera of the HST/WFPC2 (right panel) and as sampled by the WFM observations (left panel). From this comparison, it is clear that NFM observations are mandatory to obtain a large number of RV measurements from individual stars in the core of the cluster.

3. Analysis

3.1. Photometric Analysis and Selection of Target Stars

The photometric analysis has been performed on the two-dimensional (2D) image extracted from each datacube from the stacking of MUSE slices in the wavelength range 8540–8550 Å (which is the region of the calcium triplet, providing the highest signal-to-noise ratio (S/N)). To determine the position of the centroid of individual sources and identify possible blends in the MUSE data, we took advantage of catalogs obtained from HST observations, which guarantee the necessary angular resolution to properly resolve stars in the highly crowded central regions of the system. For the innermost area we used a catalog obtained from images acquired with the HST/WFPC2 Planetary Camera (having a pixel scale of 0.″046 pixel^{-1}), in the filters F439W (hereafter *B*) and F555W (hereafter *V*). The catalog has been placed on the absolute astrometric system through cross-correlation with the photometric catalog of Stetson et al. (2019),[10] and the instrumental magnitudes were

[10] For the photometric catalog, see https://www.canfar.net/storage/list/STETSON/homogeneous/MNRAS_Photometry_for_48_Clusters/.

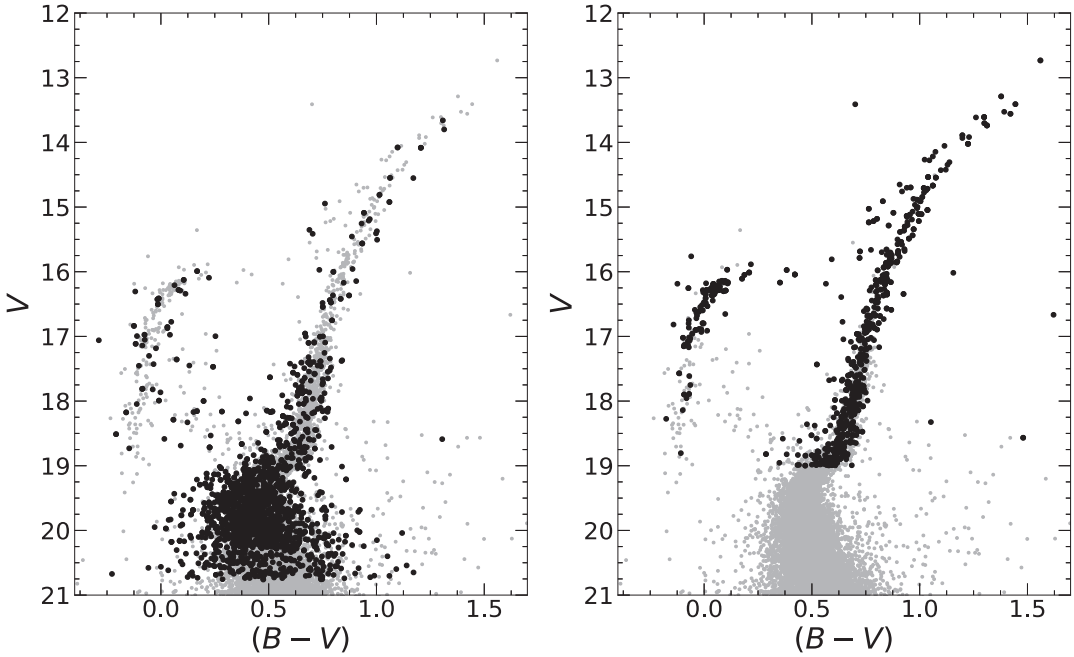

Figure 3. CMD of NGC 1904 (gray dots) obtained from the WFPC2 catalogs presented in Lanzoni et al. (2007b), with all the stars identified in the photometric analysis of the MUSE NFM and WFM images highlighted as large black dots (left and right panels, respectively).

then calibrated using the catalog discussed in Lanzoni et al. (2007b).

A quick photometric analysis of the NFM images provided us with the preliminary position of the brightest sources. Then, the cross-correlation with the HST catalog allowed us to assign to every star observed with HST an (X,Y) position in the coordinate system of the NFM images. The best-fit point-spread function (PSF) model has been determined by analyzing the brightest $\sim$10 stars in each pointing with daophot/psf (Stetson 1987). Finally, we ran daophot/allstar (Stetson 1987) to perform the PSF fitting photometry at the (X,Y) centroid position of all the HST sources with $V < 21$.[11] As a result, the PSF fitting analysis yields, for each image, the accurate position of the centroid and the instrumental magnitudes of each stellar source. As a double check, we verified that the position of the stellar centroids obtained from the PSF fitting procedure was not significantly altered by the procedure (this could happen, in principle, for the effect of a bright neighbor, or in the case of blending). Stars with centroid deviations larger than δX and $\delta Y > 0\farcs5$, with respect the HST position, have been excluded from the analysis. As a final result of the entire procedure, for each star identified in each MUSE pointing, we obtain the X and Y positions in the datacube, the R.A., Decl. absolute coordinates, and the B and V magnitudes.

A similar analysis has been performed for the WFM data set. In this case, the HST reference catalog used to identify the stellar centroids has been obtained from the combination of the two WFPC2 data sets presented in Lanzoni et al. (2007b), and different magnitude cuts have been adopted: $V < 17$ for $r < 20''$, and $V < 19$ in the region between $20''$ and $80''$ from the center. The adopted limits are brighter than those used in the analysis of the NFM data because of the brighter magnitude level reached by the WFM observations, which is clearly apparent from the comparison shown in Figure 2 and is due to shorter exposure times. Moreover, these limits depend on the radial distance from the center because, due to the low spatial resolution of the WFM observations, only brighter stars can be resolved in the higher density regions.

The $(V, B-V)$ color–magnitude diagrams (CMDs) of all the stars identified in the MUSE NFM and WFM images are overplotted to the CMD of NGC 1904 (from Lanzoni et al. 2007b) in the left and right panels of Figure 3, respectively.

3.2. Stellar Radial Velocities

As mentioned in the introduction, our approach to determine the internal kinematics of GGCs consists in measuring the RVs of resolved sources from individual stellar spectra. The procedure adopted for each MUSE datacube can be summarized as follows:

1. *Step (1): extraction of the spectra.* The spectra have been extracted at the coordinates of the stellar centroids identified during the photometric procedure (see Section 3.1). Since the targets are located in highly crowded regions, in order to limit the possible contamination from close sources, we made the conservative choice of extracting only the spectrum of the centroid spaxel of the target star and the *4* adjacent ones along the X and Y directions (hence the 5 spaxels drawing a cross centered on the centroid of the source).
2. *Step (2): normalization of the spectra.* The spectra have been normalized to the continuum estimated by a spline fitting of the portion of the spectrum in the wavelength range 6700–9300 Å. The S/N has been estimated for each spectrum as the ratio between the average of the counts and its standard deviation in the wavelength range 8000–9000 Å.
3. *Step (3): selection of template spectra.* A library of template synthetic spectra has been computed with the

[11] This magnitude cut has been set after the preliminary photometric analysis revealed that sources fainter than this limit are not reliably detected by the available NFM observations.

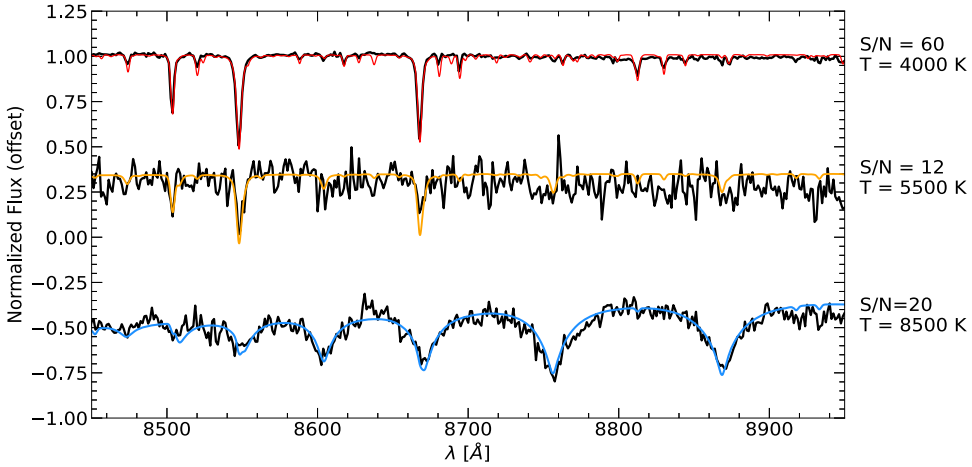

Figure 4. Examples of spectra acquired with MUSE/NFM in the region of the calcium triplet lines (in black) for different S/N values and for stars with different atmospheric parameters (see labels). The best-fit template spectra, shifted by the adopted RV value, are overplotted as colored lines. In the bottom spectrum, corresponding to an HB star with effective temperature $T = 8500$ K, the calcium triplet lines is strongly blended with the hydrogen Paschen lines. The examples shown are a good representation also of the spectra acquired with MUSE/WFM.

SYNTHE code (Sbordone et al. 2004 and Kurucz 2005), adopting the cluster metallicity (Harris 1996) and appropriate atmospheric parameters (effective temperature and gravity) according to the target evolutionary stage derived from the CMD.

4. *Step (4): measurement of RVs.* The RV of almost all the selected stars has been measured from the Doppler shift of the calcium triplet lines in the normalized spectra, in the wavelength range 8450–8740 Å. In the case of HB stars, because of the blending between the calcium triplet lines and the hydrogen Paschen lines, we used the hydrogen lines in the spectral range 8500–8930 Å. The adopted method consists in the analysis of the residuals between the observed spectrum and a set of reference spectra shifted in wavelength by quantities corresponding to different velocities, testing all the values in the range 0–400 km s^{-1}, at 0.1 km s^{-1} steps. The adopted RV is obtained from the wavelength shift that minimizes the standard deviation of the residuals.

Figure 4 shows an example of the output of this procedure. The observed spectra, with different S/N and corresponding to stars with different temperatures, are shown in black. For each of them, the figure also shows the best-fit template shifted by the adopted value of RV. As discussed above, while the calcium triplet has been used to measure the RV of the two colder stars ($T < 5000$ K; two top spectra), the hydrogen Paschen lines have been exploited for the hottest source ($T = 8500$ K; bottom spectrum). The RV values obtained from the adopted method have been compared with the results of the "standard" cross-correlation approach (Tonry & Davis 1979) implemented in IRAF, always showing good agreement independently of the spectrum S/N.

The final value of RV for each star and its uncertainty have then been computed, respectively, as the weighted mean and the weighted standard deviation of the measures obtained from the 5 extracted spaxels, after a 3σ rejection procedure aimed at removing clearly discrepant values generated by spurious effects. The relative weights of the five measures have been defined according to the fraction of the starlight sampled by each spaxel, estimated from the adopted PSF model: we assumed weight =1 for the central and most exposed spaxel and weight =0.4 and 0.5 for the 4 adjacent spaxels in the NFM and WFM samples, respectively. We used the subsamples of stars having multiple measures to check for the reliability of the RV uncertainties. By applying the method described in Section 4.1 of Kamann et al. (2016), we found that the adopted errors could be slightly overestimated (by ∼0.4 km s^{-1}). However, by taking into account that the sample of repeated measures is poor (∼80–100 stars) and the impact on the results of the work is negligible, we decided to introduce no corrective factors. The final S/N associated with each star is the weighted average of the S/N values of the considered spectra. For the following analysis, we finally selected only those stars for which the RV value was determined from at least 3 spaxels over 5, and with S/N $\geqslant 10$. The typical uncertainties are <5.0 km s^{-1} for the brightest stars ($V < 16$), while they increase for fainter magnitudes according to the corresponding decrease in S/N (see Figure 5). To produce a homogeneous final catalog, we first checked for possible systematic offsets in RV among the different MUSE pointings. To this purpose, we compared the RV values of the stars in common between two overlapping fields, always finding good agreement within the errors (only the E pointing has no objects in common with the other fields). In the cases of multiple exposures for the same star, we determined its final RV as the weighted mean of all the measures, by using the individual errors as weights.

To sample the entire radial extension of NGC 1904, we then needed to combine the MUSE RVs thus measured, with the catalog obtained by Ferraro et al. (2018b) from FLAMES and KMOS observations. We assumed as "reference" RV values those measured from the FLAMES data set because the spectral resolution of this instrument is the highest and thus provides the most accurate and reliable measures. By using the stars in common between the MUSE/WFM and the FLAMES samples, we found just a very small average offset (−1.0 km s^{-1}), which was then applied to the WFM sample for realigning it with the reference catalog. A residual −0.5 km s^{-1} offset was then identified between the RV values measured for the stars in common between the NFM and the (realigned) WFM data sets. After applying this small offset to the NFM data, we finally obtained three homogeneous samples of RVs. To create the final catalog, where every star is assigned a single RV value, we adopted the following criteria aimed at adopting the best

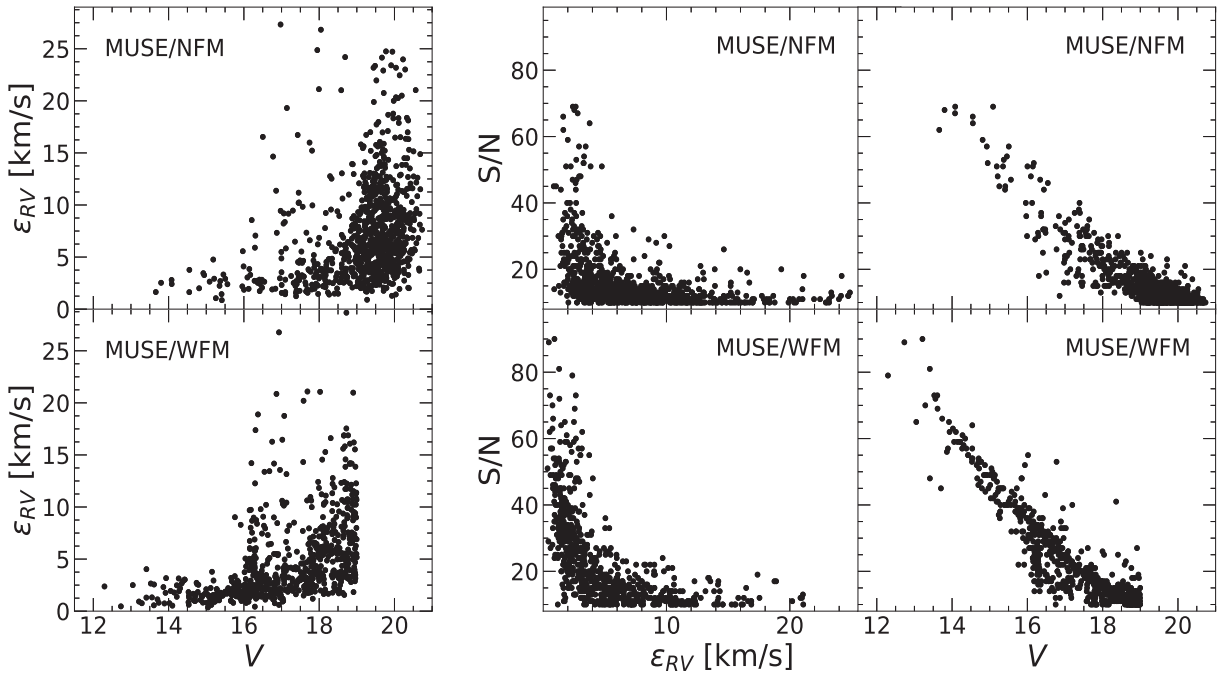

Figure 5. Left panels: RV uncertainty (ϵ_{RV}) as a function of the star magnitude for the targets of the MUSE/NFM and MUSE/WFM samples (top and bottom panel, respectively). Middle and right panels: S/N as a function of velocity error and star magnitude, for the NFM targets (top panels) and the WFM sample (bottom panels).

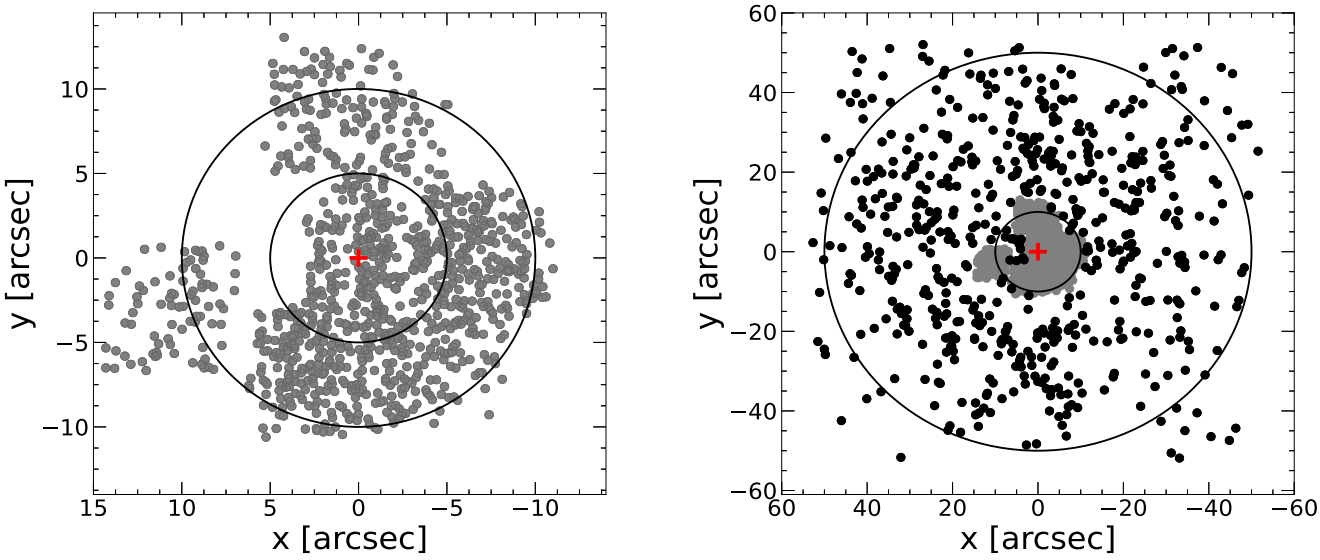

Figure 6. Left panel: map on the plane of the sky, with respect to the adopted cluster center (red cross), for all the stars with RVs measured from MUSE/NFM data. The two circles mark distances of 5″ and 10″ from the center. Right panel: the same, but for the stars with RVs obtained from the MUSE/WFM observations (black dots). The MUSE/NFM sample is also shown in gray, and the two circles mark distances of 10″ and 50″ from the center (red cross).

available measure in each case: for the stars in common between FLAMES and MUSE/WFM, we selected the RV measurements obtained with FLAMES; for the stars in common between KMOS and MUSE, we used the MUSE measures; and in the case of common targets between MUSE/WFM and MUSE/NFM, we used the NFM values.

The final catalog lists 1726 individual stars with measured RV, with each data set contributing as follows:

1. The MUSE/NFM catalog consists of 946 measures for sources located between 0.″3 and 15.″7 from the cluster center (Figure 6, left panel). They sample the magnitude range $13.5 < V < 21$, and their position in the $(V, B-V)$ CMD is shown in the left panel of Figure 7 (black dots).
2. The MUSE/WFM data set consists of 587 stars located between 2.″3 and 66.″5 from the cluster center (black dots in the right panel of Figure 6) and with magnitudes $12 < V < 19$ (red crosses in the left panel of Figure 7).
3. The FLAMES/KMOS sample consists of 193 stars, sampling the radial region beyond ∼20″, out to 774″ from the cluster center (see Ferraro et al. 2018b).

3.3. Contamination Estimate of the MUSE Targets

Although in NGC 1904 we do not expect significant contamination from the foreground Galactic field sources, the MUSE observations presented in this paper sample the core of

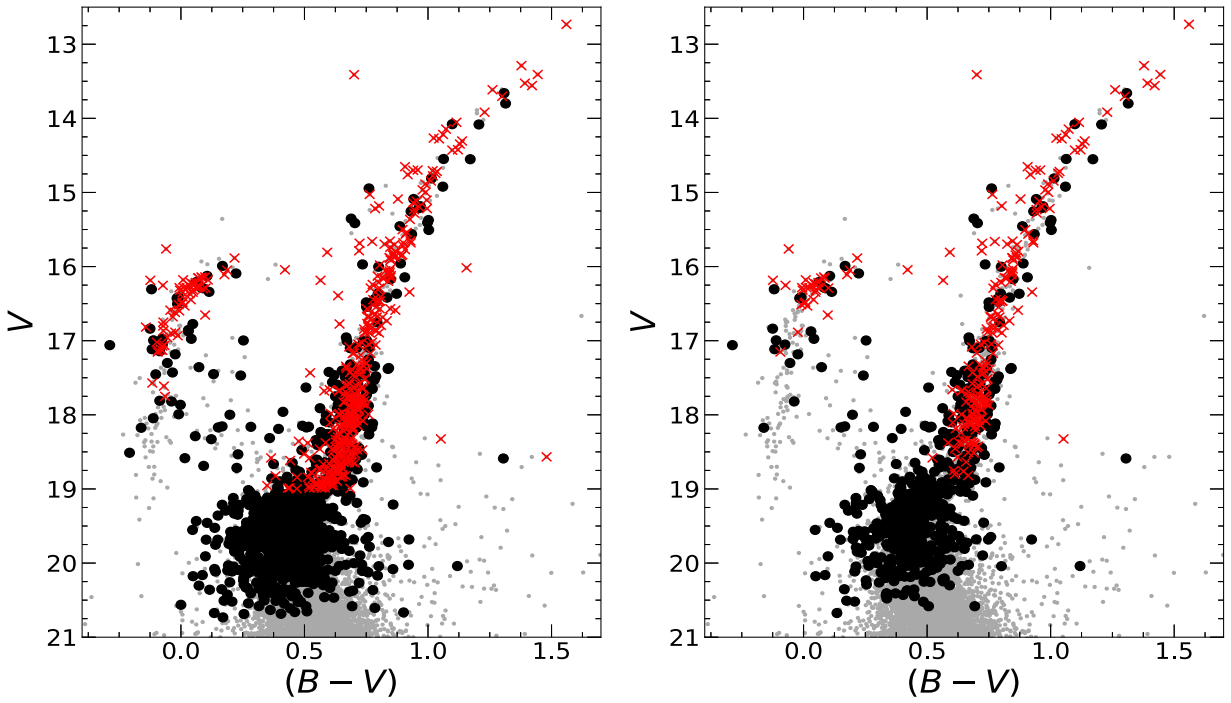

Figure 7. Left panel: CMD of NGC 1904 obtained from the photometric catalog discussed in Lanzoni et al. (2007b) (gray dots), with the stars having RVs measured from the MUSE observations marked as black circles (NFM sample) and red crosses (WFM data set). Right panel: the same, but only for the stars used to determine the internal kinematics of NGC 1904, i.e., stars with RV uncertainty $\epsilon_{RV} < 10$ km s^{-1}, S/N > 10, and contamination ratio $C \leqslant 0.05$.

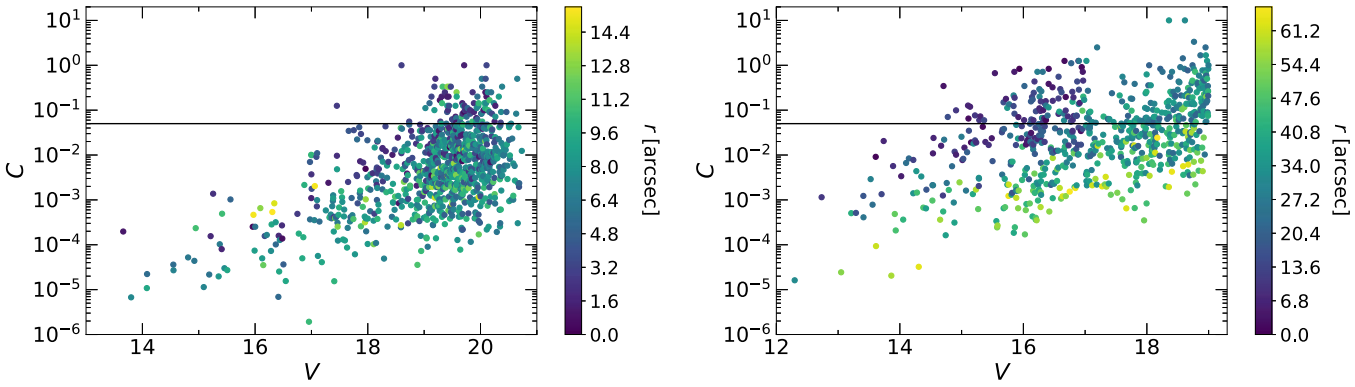

Figure 8. Contamination parameter (C; see text) as a function of magnitude, for the MUSE/NFM targets (left panel) and the MUSE/WFM sources (right panel). The color scale indicates the distance of the targets from the cluster center (see color bars). The black line flags the adopted contamination threshold: only targets with $C \leqslant 0.05$ have been used to determine the internal cluster kinematics.

the cluster, where stellar crowding is critical. Hence, the RV value measured for a given star might be affected by the presence of bright neighboring sources. In turn, this can impact the final results, in terms of velocity dispersion and systemic rotation of the cluster. To quantify this effect and select the spectra contributed by the light of individual stars only, we implemented a procedure aimed at estimating the level of contamination suffered by each MUSE target.

We considered all the sources listed in the HST catalogs used for the photometric analysis and modeled each of them with the adopted MUSE PSF function (see Section 3.1). For every MUSE target, this allowed us to estimate the amount of light in the central spaxel contributed by the star under analysis and the surrounding objects. Using the entire HST catalogs (instead of only the MUSE targets with measured RV) guarantees that we are taking into account a complete list of sources, including stars that are not identified (because they are too faint) or are blended in the MUSE observations, as well as stars that are located just beyond the edges of the MUSE fields. From this analysis we then quantify the level of contamination of each MUSE target through the contamination parameter (C) defined as the ratio between the fraction of light contributed by the first contaminant and that of the target under analysis, where the first contaminant is the neighboring source providing the largest contribution to the central spaxel light after the target itself.

Figure 8 shows the parameter C estimated for all the MUSE targets as a function of the magnitude, with the color code illustrating the dependence on the distance from the cluster center. As expected, the most contaminated stars (large values of C) are the faint ones. Moreover, the contamination from neighboring stars is more severe for the observations acquired at lower spatial resolution (WFM, right panel), with respect to those performed with AO correction (NFM, left panel). The

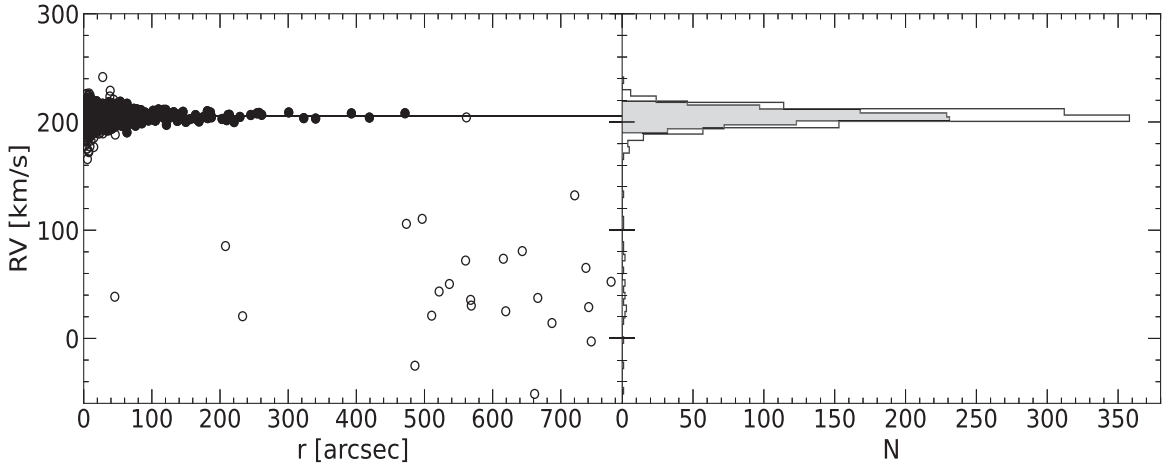

Figure 9. Left panel: RVs of the final sample of (1078) selected stars as a function of their distance from the cluster center. The filled circles flag those used to determine the cluster systemic velocity (black solid line), while the open circles mark those rejected by the 3σ-clipping algorithm. The number distribution of the targets used for the systemic velocity is plotted as a filled gray histogram and compared to that of the entire sample (open histogram) in the right panel.

figure also illustrates that, to discriminate isolated from contaminated targets, it is more efficient to select a threshold in C, instead of a cut in magnitude; indeed, this allows us to keep in the sample faint but isolated stars, as well as to reject targets that, in spite of being relatively bright, are contaminated by neighbors. For the following analysis, we made the conservative choice of keeping in the sample only the MUSE targets with contamination parameter smaller than 5% ($C \leqslant 0.05$), for which we estimate that neighboring stars have a negligible impact on the measured RV. The final sample includes 857 stars in the NFM data set and 351 stars observed with MUSE/WFM.

4. Results

To properly determine the internal kinematics (systemic velocity, velocity dispersion profile, and rotation curve) of NGC 1904 from the available data set, we further selected the sample by considering only stars with RV uncertainty smaller than 10 km s^{-1} and S/N higher than 10. This brought the final sample to a total of 1078 RV measures, for individual stars located in a large range of radial distances, from $0\farcs3$ out to $\sim 774''$ (about 14 3D half-mass radii, assuming the half-mass radius of the system $r_h = 56\farcs7$ presented in Miocchi et al. 2013) from the cluster center. The CMD distribution of the selected MUSE target is shown in the right panel of Figure 7.

4.1. Systemic Velocity

Figure 9 shows the distribution of the 1078 RVs measured in NGC 1904 as a function of the distance from the cluster center. The population of cluster members is clearly distinguishable as a narrow, strongly peaked component, which dominates the sample at RV ~ 200 km s^{-1}. To carefully determine the value of the cluster systemic velocity ($V_{\rm sys}$), we rejected obvious outliers, selecting only the targets with RV in the range 190 km s^{-1} $<$ RV $<$ 220 km s^{-1}. Under the assumption that the RV distribution is Gaussian, we used a maximum likelihood approach (e.g., Walker et al. 2006) to estimate the cluster systemic velocity and its uncertainty. By applying the selection criteria described above and a 3σ-clipping procedure, a sample of 998 RV measures has been used for the estimate of $V_{\rm sys}$. These are marked as black filled circles in the left panel of Figure 9, and their distribution is shown in gray in the right panel of the same figure. The resulting value is $V_{\rm sys}$ 205.4 ± 0.2 km s^{-1}, in good agreement with previous determinations, e.g., 205.8 ± 0.4 km s^{-1} (Harris 1996), 205.78 ± 0.54 km s^{-1} (D'Orazi et al. 2015), 205.4 ± 0.6 km s^{-1} (Ferraro et al. 2018b), and 205.6 ± 0.2 km s^{-1} (Baumgardt & Hilker 2018). Different, but still reasonable, assumptions about the cuts in RV, error, and contamination parameter produce no significant variations in this result. We also verified that using only the MUSE/NFM and MUSE/WFM catalogs individually provides perfectly consistent values of $V_{\rm sys}$, as illustrated in Table 2. In the following, we will use $V_r = {\rm RV} - V_{\rm sys}$ to indicate the RV values referred to the cluster systemic velocity.

Table 2
Systemic Velocity of NGC 1904

Catalog	$r_{\rm min}$ (arcsec)	$r_{\rm max}$ (arcsec)	N	N_V	$V_{\rm sys}$ km s^{-1}
MUSE/NFM	0.3	15.7	599	553	205.2 ± 0.3
MUSE/WFM	4.2	64.1	286	276	205.7 ± 0.4
MUSE + FLAMES/KMOS	0.3	773.7	1078	998	205.4 ± 0.2

Note. For the catalog including only MUSE/NFM targets, that of MUSE/WFM stars, and the global catalog obtained after the combination of the previous two with the catalog discussed in Ferraro et al. (2018b), the table lists the minimum and maximum distances from the cluster center sampled by the observed stars ($r_{\rm min}$ and $r_{\rm max}$, respectively), the total number of stars after all selections (i.e., RV uncertainty $\epsilon_{\rm RV} < 10$ km s^{-1}, S/N > 10, and $C \leqslant 0.05$), the number of stars used for the determination of the systemic velocity (N_V), and the resulting value of $V_{\rm sys}$ with its 1σ uncertainty.

4.2. Second Velocity Moment Profile

The dispersion of the measured RVs about the cluster systemic velocity, determined at different radial distances from the center, provides the second velocity moment profile of the system, $\sigma_{II}(r)$. Under the assumption of no relevant rotation, this is a good approximation of the projected velocity dispersion profile, $\sigma_P^2(r)$. In fact,

$$\sigma_P^2(r) = \sigma_{II}^2(r) - A_{\rm rot}^2(r), \quad (1)$$

where $A_{\rm rot}$ is the rotation curve amplitude. Indeed, preliminary evidence of rotation was recently detected in the external

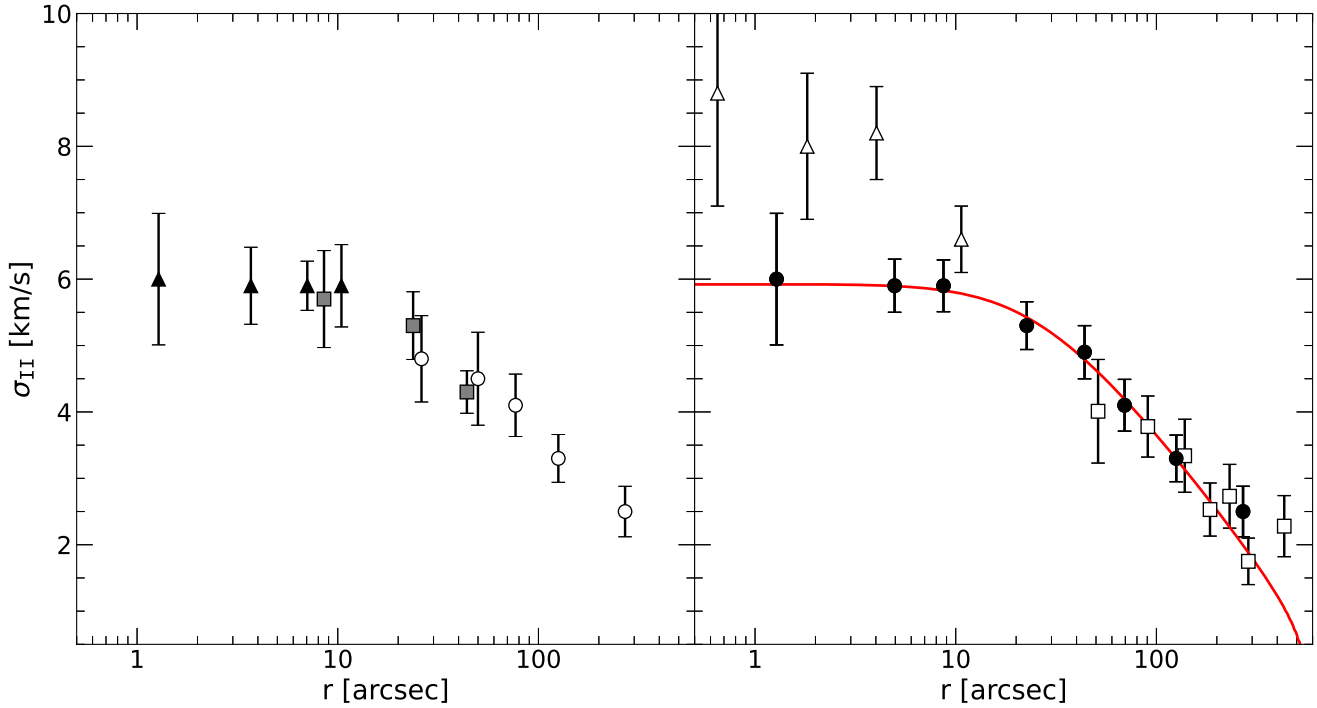

Figure 10. Left panel: second velocity moment profiles obtained from the three considered catalogs separately: MUSE/NFM data (black triangles), MUSE/WFM data (gray squares), and the catalog presented in Ferraro et al. (2018b; open circles). Right panel: second velocity moment profile of NGC 1904 obtained from the individual RVs of all the stars included in the combined MUSE/NFM, MUSE/WFM, and FLAMES data set (filled circles). The open triangles represent the profile derived by Lützgendorf et al. (2013), from the line broadening of integrated-light spectra in the inner regions, while the open squares have been obtained from individual RVs by Scarpa et al. (2011) in the outskirts. The red solid line shows the King model that best fits the star density profile of NGC 1904, as obtained in Miocchi et al. (2013).

region of NGC 1904 (Ferraro et al. 2018b), and it is confirmed in the present study, as discussed in the next section. Hence, the correct determination of the velocity dispersion profile of this system requires the evaluation of the strength of rotation and its radial variation. However, the second velocity moment profile is still worth determining since it offers the opportunity of a first-order comparison with previous results in the literature that ignored the effects of the cluster rotation.

As usual, the radial profile has been obtained by splitting the surveyed area into a set of concentric annuli, at increasing distance from the cluster center, chosen as a compromise between a good radial sampling and a statistically significant number of stars (at least 20–30). In each radial bin, obvious outliers (like field stars, having RVs in clear disagreement with the cluster distribution in that radial interval) have been excluded from the analysis, and a 3σ-clipping algorithm about the cluster systemic velocity has been applied to further clean the sample. Then, $\sigma_{II}(r)$ has been computed from the dispersion of the values of V_r measured for all the remaining stars in each annulus, by following the maximum likelihood method described in Walker et al. (2006; see also Martin et al. 2007; Sollima et al. 2009). The error is estimated following the procedure outlined in Pryor & Meylan (1993).

For the sake of illustration, the left panel of Figure 10 shows the second velocity moment profiles obtained from the three considered catalogs, separately: MUSE/NFM and MUSE/WFM discussed in this study (black triangles and gray squares, respectively), and the FLAMES-KMOS catalog of Ferraro et al. (2018b; open circles). Table 3 lists the values obtained. The figure illustrates how the three catalogs provide complementary coverages of different radial portions of the cluster, and

Table 3
Second Velocity Moment Profiles Obtained from the MUSE/NFM and MUSE/WFM Data Sets, Separately, and Using the Combined Catalog of MUSE/NFM, MUSE/WFM, and FLAMES Data

r_i (arcsec)	r_e (arcsec)	r_m (arcsec)	N	σ_{II} (km s^{-1})	$\epsilon_{\sigma_{II}}$ (km s^{-1})
MUSE/NFM					
0.01	2.00	1.28	31	6.00	0.99
2.00	5.00	3.69	121	5.90	0.58
5.00	9.00	7.05	294	5.90	0.37
9.00	15.00	10.43	125	5.90	0.62
MUSE/WFM					
0.01	15.00	8.54	35	5.70	0.73
15.00	30.00	23.74	88	5.30	0.51
30.00	66.00	44.00	187	4.30	0.32
Combined Catalog					
0.01	2.00	1.28	31	6.00	0.99
2.00	7.00	4.96	269	5.90	0.40
7.00	11.00	8.69	259	5.90	0.39
11.00	35.00	22.58	203	5.30	0.36
35.00	55.00	43.84	138	4.90	0.40
55.00	100.00	69.37	73	4.10	0.39
100.00	170.00	125.57	43	3.30	0.35
170.00	600.00	270.13	23	2.50	0.38

Note. The first three columns list the internal, external, and mean radii of each adopted radial bin (r_i, r_e, and r_m, respectively), with the mean radius computed as the average distance from the center of all the stars in the bin (N, fourth column). The last two columns list the second velocity moment and its uncertainty in each bin, respectively.

that the resulting kinematic profiles are in very good agreement with each other. The final second velocity moment profile of NGC 1904, as obtained from the combined catalog, is shown in the right panel of Figure 10 (filled circles) and listed in Table 3. Its stays flat in the central regions ($r \lesssim 10''$), with a central value of $\sim$6.0 km s^{-1}, and then decreases in the outer regions, as usually observed.

In the right panel of Figure 10, this profile is compared with that published in Lützgendorf et al. (2013; open triangles), which was obtained by measuring the line broadening of integrated-light spectra at $r < 10''$, and with that obtained in Scarpa et al. (2011; open squares) from individual RVs in the outer cluster region. As can be seen, while the profiles agree quite well at large distances from the center, the value measured in the innermost core is significantly larger than that presented here, and it was interpreted as the signature of a $\sim$3000 $M_\odot$ IMBH. This discrepancy is qualitatively similar, although significantly less pronounced, to that found in the case of NGC 6388, where it was ascribed to the presence of two bright central stars with opposite RVs provoking a spurious broadening of the (integrated-light) spectral lines and, in turn, an overestimate of the velocity dispersion in the cluster innermost region (see Lanzoni et al. 2013). In the innermost 10″ of NGC 1904 we measured the RV for almost 530 stars. Hence, we conclude that the result presented in the right panel of Figure 10 is solid. It indicates a central value of the second velocity moment $\sim$25% smaller than that quoted in Lützgendorf et al. (2013; $\sigma_0 = 6$ km s^{-1} instead 8 km s^{-1}), and it excludes the presence of a central IMBH, at least an IMBH massive enough to produce a detectable perturbation in the second velocity moment profile. We also note that, in spite of having adopted the results of Lützgendorf et al. (2013), the best-fitting N-body model to the surface density and line-of-sight velocity dispersion profiles of NGC 1904 determined by Baumgardt & Hilker (2018) suggests a central value of $\sim$6.5 km s^{-1} (see their Figure E1), which is in good agreement with our analysis.

4.3. Systemic Rotation

A significant signature of rotation has been found in the outer regions of NGC 1904, from the analysis of individual RVs by Ferraro et al. (2018b). This is consistent with the findings presented in Scarpa et al. (2011), who measured a cluster rotational velocity of 1.1 km s^{-1} within 3′ from the center, with respect to an axis with position angle PA = 85° (as measured from north toward east), from a total sample of $\sim$150 RVs. Signatures of rotation in the plane of the sky, as determined from the analysis of PMs, appear more controversial. A signal of rotation has been presented in the recent compilation of Vasiliev & Baumgardt (2021), while Sollima et al. (2019) classified the cluster rotation as uncertain because, although a signal was detected at more than the 3σ significance level, the GC failed one of the tests performed to check for spurious rotation effects. Thanks to the large sample of MUSE individual RVs presented in this paper, we are now able to explore the rotational properties of NGC 1904 over its entire radial extension. On the other hand, the analysis of the Gaia EDR3 offers the opportunity to study the kinematics also in the plane of the sky, thus providing a comprehensive analysis of the cluster rotation.

For the line-of-sight direction, we adopted the same approach followed in Ferraro et al. (2018b) and Lanzoni et al. (2018a, 2018b) and described, e.g., in Bellazzini et al. (2012; see also Lanzoni et al. 2013). The method consists in splitting the RV data set into two subsamples by means of a separation line passing through the cluster center and with PA varying between 0° (north direction) and 180° (south direction), in steps of 10°, with PA = 90° corresponding to the east. For each value of PA, the difference between the mean velocities of two groups of stars ($\Delta V_{\rm mean}$) is measured and recorded. By construction, the method requires a sample of RVs symmetrically distributed on the plane of the sky, while it cannot be applied if large areas remain unsampled by the available data set. The presence of rotation along the line of sight is expected to produce the following set of observable properties:

1. By progressively rotating the separating line from north to south, $\Delta V_{\rm mean}$ is expected to draw a coherent sinusoidal dependence on PA. The maximum/minimum of this curve provides the PA of the rotation axis (PA_0), since it corresponds to the strongest separation in approaching and receding subsamples. The absolute value of the maximum/minimum of this curve corresponds to twice the rotation amplitude ($A_{\rm rot}$).
2. The projected spatial distribution is expected to be flattened in the direction of the rotation axis.
3. The subsamples of stars on each side of the rotation axis are expected to show not only different mean velocities (as quantified by $\Delta V_{\rm mean}(PA_0)$) but also different cumulative V_r distributions. To quantify the statistical significance of such difference, we used three estimators: the probability that the RV distributions of the two subsamples are extracted from the same parent family is evaluated by means of a Kolmogorov–Smirnov test, while the statistical significance of the difference between the two sample means is estimated with both the Student's t-test and a maximum likelihood approach.

We applied this procedure to our RV sample, in three concentric annuli around the cluster center with sufficiently symmetric spatial sampling (we thus excluded the innermost 10″; see the left panel of Figure 6). The results are plotted in Figure 11. In all the considered annuli, we find well-defined sinusoidal behaviors of $\Delta V_{\rm mean}$ as a function of PA (left panels), asymmetric distributions of V_r as a function of the projected distance from the rotation axis XR (middle panels), and well-separated cumulative V_r distributions for the two samples on either side of the rotation axis (right panels). The reliability of these systemic rotation signatures is also confirmed by the values of the Kolmogorov–Smirnov and t-Student probabilities and by the significance level of different sample means obtained from the maximum likelihood approach (see the three last columns in Table 4), thus providing a solid confirmation of a coherent global rotation of the system. Averaging values of PA_0 weighted by the number of stars in each radial bin, we obtained $PA_0 = 98°$, which is adopted as the global PA for the cluster rotation axis. This locates the rotation axis essentially aligned to the east–west direction, dividing the observed data set into a northern subsample with positive mean V_r and a southern approaching subsample (with negative mean V_r). By fixing PA_0 to this value, we applied the described procedure to all stars measured at $r > 5''$ (for the reason discussed in the next paragraph), finally obtaining the diagnostic plots shown in the three bottom panels of Figure 11 and the results listed in the bottom line of Table 4.

The peculiar behavior of the innermost core.—In performing the analysis of the rotation curve, we discovered a peculiar

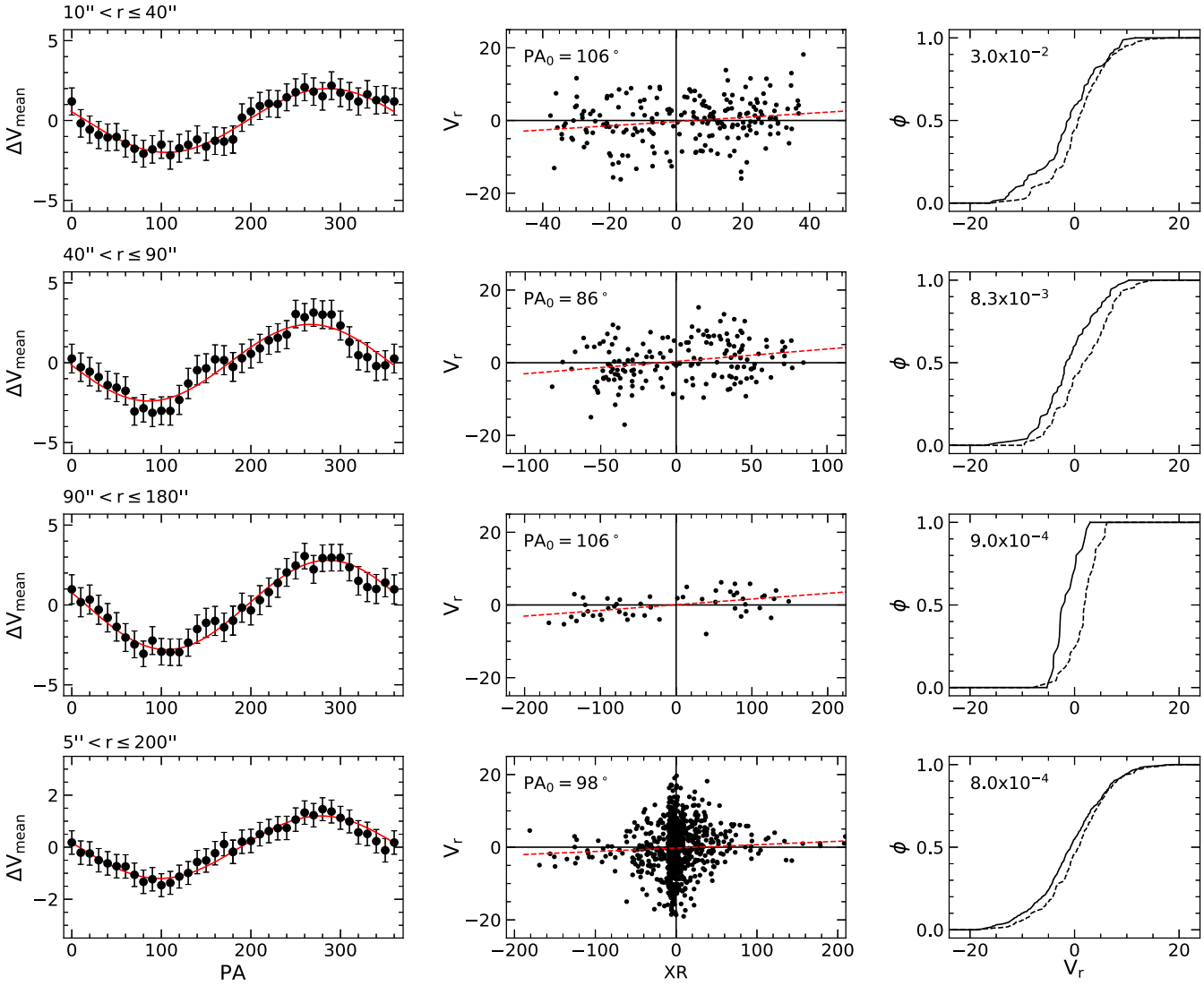

Figure 11. Diagnostic diagrams of the rotation signature detected in three concentric annuli at different distances from the cluster center (three top panels; see labels in their upper left corner), and considering the entire sample with $r > 5''$ (bottom panels). For each bin the left panels show the difference between the mean RV on each side of a line passing through the center with a given PA, as a function of PA itself. The solid line is the sine function that best fits the observed patterns. The middle panels show the distribution of the radial velocities V_r as a function of the projected distances from the rotation axis (XR) in arcseconds. The PA of the rotation axis (PA_0) is labeled in each panel. The red dashed lines are the least-squares fits to the data. The right panels show the cumulative RV distributions for the sample of stars with XR < 0 (solid line) and for that with XR > 0 (dotted line). The Kolmogorov–Smirnov probability that the two samples on each side of the rotation axis are drawn from the same parent distribution is also labeled.

Table 4
Rotation Signatures Detected in Circular Annuli around the Cluster Center and Global Rotation Found in NGC 1904 Using the Entire Sample with $r > 5''$ (Bottom Line)

r_i	r_e	r_m	N	PA_0	A_{rot}	P_{KS}	P_{Stud}	n-σ_{ML}
10	40	27.3	206	106	1.0	3.0×10^{-2}	>95.0	2.2
40	90	54.7	165	86	1.2	8.3×10^{-3}	>99.8	3.1
90	180	122.2	51	106	1.4	9.0×10^{-4}	>99.8	4.0
5	800	34.6	881	98	0.6	8.0×10^{-4}	>99.0	2.9

Note. For each radial bin the table lists the inner and outer radius (r_i and r_e) in arcseconds, the mean radius and the number of stars in the bin (r_m and N, respectively), the PA of the rotation axis (PA_0), the rotation amplitude (A_{rot}), the Kolmogorov–Smirnov probability that the two samples on each side of the rotation axis are drawn from the same parent distribution (P_{KS}), the t-Student probability that the two RV samples have different means (P_{Stud}), and the significance level (in units of n-σ) that the two means are different following a maximum likelihood approach (n-σ_{ML}).

feature that needs to be further investigated. Since the sampling of the innermost $3''$ is sufficiently symmetric (see the left panel of Figure 6), we applied the described procedure also in this region, leaving the PA free to vary between 0° and 180°. We found evidence of a rotation signal for $PA_0 = 93°$, but the rotation pattern is just opposite to that found for $r > 10''$: the northern subsample has negative mean V_r (it is approaching), while the stars observed in the southern hemisphere are preferentially receding from the observer (positive mean V_r). Admittedly, the detection of this effect is based on a just limited number of stars (∼60) and the statistical significance is not high (e.g., t-Student probability that the two RV samples have different means is $P_{Stud} \sim 90\%$, only). Figure 12 shows a MUSE/NFM image zoomed in to the innermost $3''$ from the center with the considered stars flagged with two different colors: in red those receding from the observer, in green the approaching ones. The difference in the mean RV of the two

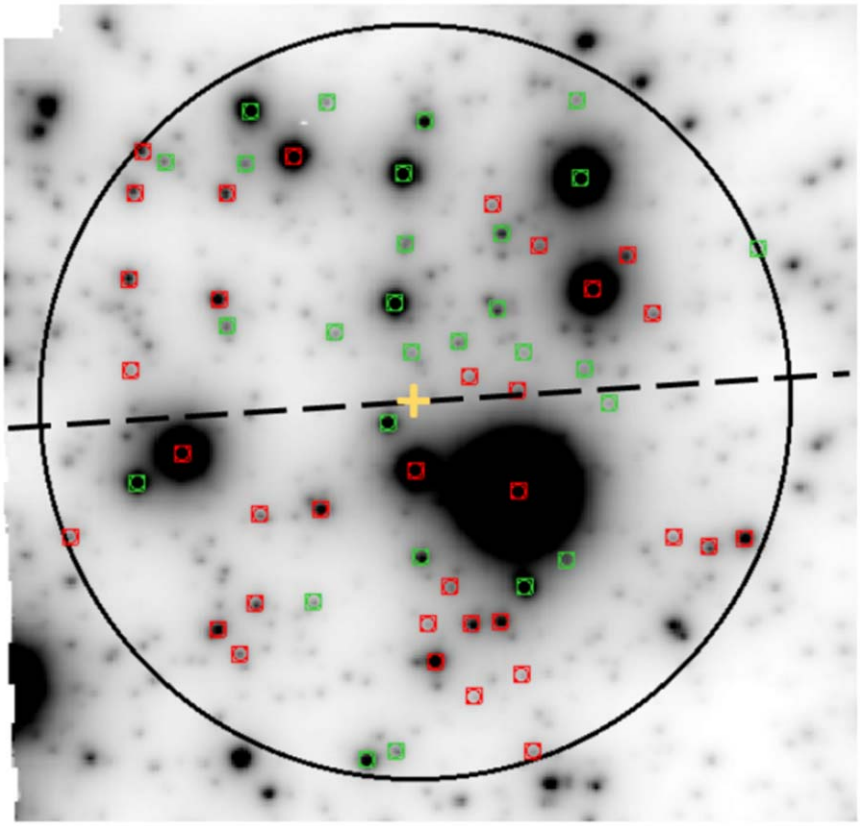

Figure 12. Zoomed-in portion of the reconstructed MUSE/NFM image in the innermost region of NGC 1904. The black circle is centered on the cluster center (yellow cross) and has a radius of 3″. North is up, east is left. Red symbols mark stars with RV larger than the cluster systemic velocity (receding stars), while green symbols mark the stars approaching the observer. The orientation ($PA_0 = 93°$) of the axis that maximizes the difference between the mean RVs of the two subsamples is also shown as a dashed line.

samples is apparent also by eye. If confirmed, this could represent the detection of a kinematically decoupled core. A similar kinematic feature has been detected so far only in M15 (van den Bosch et al. 2006; Bianchini et al. 2013; Kamann et al. 2018b; Usher et al. 2021). It has been suggested that stellar interactions with massive binary black holes (Mapelli et al. 2005) may produce this feature, but the viability of this scenario in M15 is unclear, and further investigations of other dynamical scenarios and the possible role of core collapse are necessary. In any case, the statistics is admittedly too poor to draw any firm conclusion. We therefore avoid any further discussion of this feature and exclude the stars located at $r < 3''$ from the following analysis.

4.4. Line-of-sight Rotation Curve

We built the rotation curve of NGC 1904 by splitting the RV sample into four intervals sampling increasing values of XR on both sides of the rotation axis. Following Walker et al. (2006), Sollima et al. (2009), and Lanzoni et al. (2018a), we used a maximum likelihood method to determine the mean velocity of all the stars belonging to each XR bin. The errors have been estimated following Pryor & Meylan (1993). The resulting rotation curve is shown in Figure 13 and presented in Table 5. It clearly shows the expected shape, with a steep increasing trend in the innermost regions and a maximum value followed by a soft decreasing behavior outward. The observed trend is well reproduced by an analytic function (Lynden-Bell 1967) appropriate for cylindrical rotation:

$$V_{\rm rot} = \frac{2A_{\rm peak}}{{\rm XR}_{\rm peak}} \frac{\rm XR}{1 + ({\rm XR}/{\rm XR}_{\rm peak})^2}, \quad (2)$$

where $A_{\rm peak}$ and ${\rm XR}_{\rm peak}$ are the maximum rotation amplitude and its distance from the rotation axis, respectively. The red solid line in Figure 13 shows the model computed for a maximum amplitude of $\sim$1.5 km s^{-1} at ${\rm XR}_{\rm peak} \sim 70''$ from the rotation axis, approximately corresponding to the 3D half-mass radius (or nearly 2 projected half-mass radii, adopting the value $R_{\rm h} = 41\farcs7$ quoted in Miocchi et al. 2013). The evidence of systemic rotation of NGC 1904 along the line of sight is apparent. Rotation patterns as clear as that found here are now detected in a growing number of cases (NGC 4372 in Kacharov et al. 2014, 47 Tucanae in Bellini et al. 2017, M5 by Lanzoni et al. 2018a, NGC 5986 by Lanzoni et al. 2018b, NGC 6362 by Dalessandro et al. 2021a; see also Bianchini et al. 2013; Vasiliev & Baumgardt 2021).

4.5. Velocity Dispersion Profile

Once the line-of-sight rotation curve is determined, the projected velocity dispersion profile, $\sigma_P(r)$, can be finally obtained from the dispersion of the measured RVs after subtraction of the ordered motion contribution. We thus assigned to each star the mean rotational velocity of the XR shell to which it belongs and subtracted this value from the measured RV. Then, we repeated the maximum likelihood

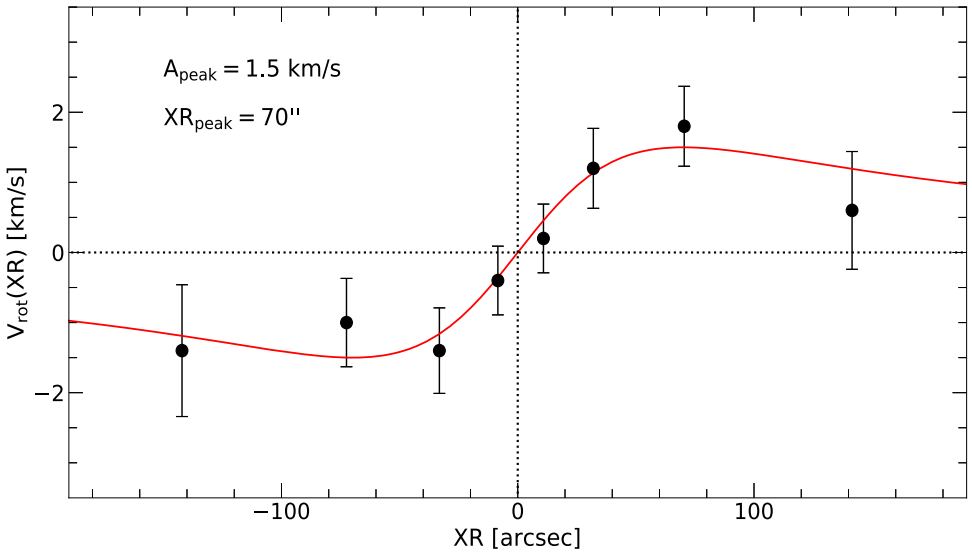

Figure 13. Rotation curve of NGC 1904. The black circles mark the stellar mean velocity as a function of the projected distance on either side of the rotation axis (XR) for the intervals listed in Table 5. The red line, which well reproduces the observed curve, is the model shown in Equation (2), with $A_{\rm peak} = 1.5$ km s^{-1} and $\rm XR_{peak} = 70''$.

Table 5
Line-of-sight Rotation Curve of NGC 1904

$\rm XR_i$	$\rm XR_e$	$\rm XR_m+$	$N+$	$V_{\rm rot}+$	ϵ_{V+}	$\rm XR_m-$	$N-$	$V_{\rm rot}-$	ϵ_{V-}
5	20	10.88	139	0.20	0.49	−8.41	212	−0.40	0.49
20	50	31.99	102	1.20	0.57	−33.17	78	−1.40	0.61
50	110	70.46	36	1.80	0.57	−72.49	28	−1.00	0.63
110	200	141.51	9	0.60	0.84	−142.11	11	−1.40	0.94

Note. Rotation curve of NGC 1904. For four intervals of projected distances from the rotation axis (XR), the table lists the inner and outer absolute limits of each bin ($\rm XR_i$ and $\rm XR_e$) in arcseconds, mean distance, number of stars, and average velocity and its error (in km s^{-1}) on the positive side of the XR axis (Columns (3)–(6)) and on its negative side (Columns (7)–(10)).

procedure described in Section 4.2 to determine the projected velocity dispersion profile of NGC 1904 in circular concentric shells. The result is shown in Figure 14 (red circles) and listed in Table 6. For the sake of comparison we also show the radial profile of the second velocity moment (black circles) determined in Section 4.2 and listed in Table 3.

By construction the velocity dispersion is systematically smaller than the second velocity moment in every bin. However, the differences are small and always within the errors, as expected in the case of a pressure-supported system. Indeed, in spite of a clean rotation signal, the rotational velocity is small, and it is smaller than the velocity dispersion in all radial bins, confirming that the kinematics of NGC 1904 is dominated by nonordered motions.

4.6. Rotation in the Plane of the Sky

In order to study the rotation of the cluster in the plane of the sky, we used the most recent data release (EDR3) of the Gaia mission (Gaia Collaboration et al. 2021). Using this data set, Vasiliev & Baumgardt (2021) have detected a signal of rotation in NGC 1904 at a more than 3σ confidence level and with a maximum amplitude of $\sim$2.0 km s^{-1} at $\sim 2'$. In a previous analysis using both line-of-sight velocities and PMs from Gaia DR2, Sollima et al. (2019) quoted a rotation velocity amplitude of 2.24 ± 0.46 km s^{-1} but classified the rotation signal as uncertain because the cluster failed one of the tests performed against random or systematic effects (see their Table 1). Here we independently analyzed the Gaia EDR3 data searching for signature of rotation in the plane of the sky. We first applied the following selection criteria on the astrometric and photometric quality indicators (given in the Gaia archive and discussed in Fabricius et al. 2021; Lindegren et al. 2021; Riello et al. 2021), in order to use the stars with the most reliable astrometric measures: (i) RUWE[12] < 2.4; (ii) astrometric_excess_noise[13] < 2; (iii) phot_bp_rp_excess_factor[14] $< 2.6 + 0.12$ $(\rm BP - RP)^2$, where BP and RP are the magnitude in the BP and RP bands, respectively; (iv) $\rm G < 19$; (v) PM errors < 0.06 mas yr^{-1} for stars with $\rm G < 16$, while for $\rm G > 16$ we have divided the sample into bins of distance (0″–50″, 50″–100″, 100″–150″, and distance >150″) and bins of magnitude 0.5 G magnitude wide, and we have excluded the stars with PM errors larger than 1σ of the local mean error in each bin. Finally, we selected stars within 0.2 mas yr^{-1} (corresponding to about $2 \times \sigma_0$ at the distance of NGC 1904) from the absolute motion (Vasiliev & Baumgardt 2021) in the vector-point diagram (VPD; see the left panel of Figure 15). The final sample includes 437 stars located between 7″ and 1338″ from the center. Their $\mu_\alpha cos\delta$

[12] RUWE is the renormalized unit weight error (for astrometry) discussed in Lindegren et al. (2021).
[13] It is the excess noise of the source, and it measures the disagreement, expressed as an angle, between the observations of a source and the best-fitting standard astrometric model.
[14] It is the sum of the integrated BP and RP fluxes divided by the G flux. It gives an indication of the consistency between the three fluxes (for more details see Riello et al. 2021).

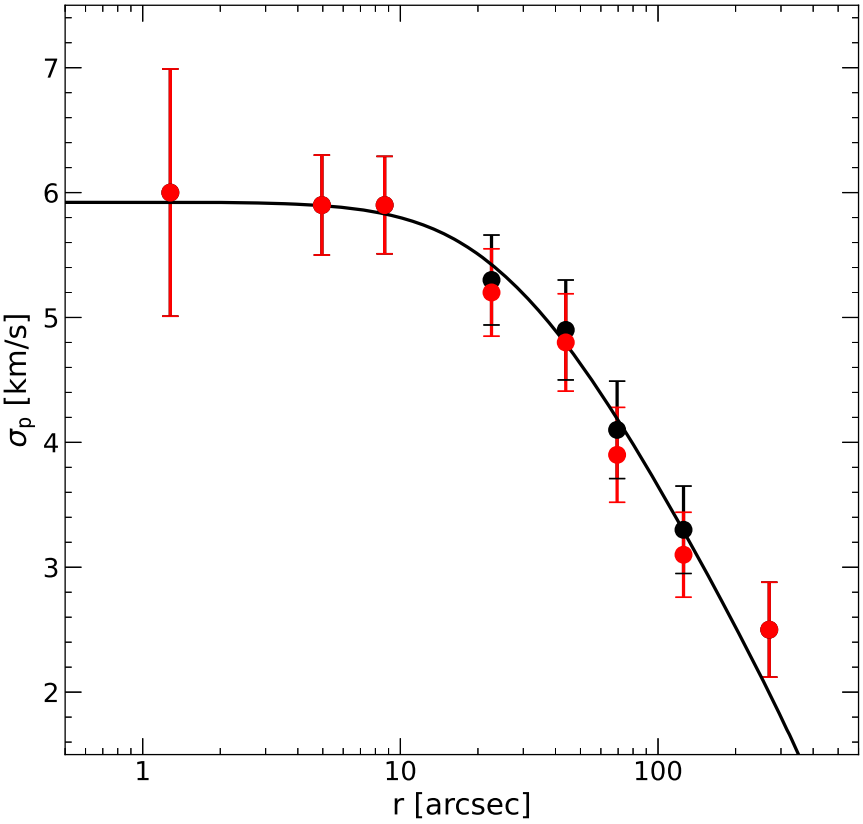

Figure 14. Velocity dispersion profile of NGC 1904 (red circles) obtained after subtracting the contribution of rotation in all radial bins. The second velocity moment profile (the same as in Figure 10), which includes the effects of both rotation and velocity dispersion in each circular shell, is also shown for comparison (black circles). The solid line shows the King model that best fits the projected density distribution of NGC 1904 by Miocchi et al. (2013).

Table 6
Velocity Dispersion Profile of NGC 1904

r_i (arcsec)	r_e (arcsec)	r_m (arcsec)	N	σ_P (km s^{-1})	$\epsilon_{\sigma P}$ (km s^{-1})
0.01	2.00	1.28	31	6.00	0.99
2.00	7.00	4.96	269	5.90	0.40
7.00	11.00	8.69	259	5.90	0.39
11.00	35.00	22.58	203	5.20	0.35
35.00	55.00	43.84	138	4.80	0.39
55.00	100.00	69.37	73	3.90	0.38
100.00	170.00	125.57	43	3.10	0.34
170.00	600.00	270.13	23	2.50	0.38

Note. The first four columns list the internal, external, mean radii, and number of stars of each adopted radial bin (r_i, r_e, r_m, and N, respectively). The last two columns list the velocity dispersion and its uncertainty in each bin, respectively.

and μ_δ PMs are shown (black dots) in the VPD in the left panel of Figure 15, while their distribution on the plane of the sky is plotted in the right panel of the same figure. The PMs measured for the selected stars and their corresponding uncertainties have been converted into a Cartesian reference frame centered on the cluster center using Equation (2) of Gaia Collaboration et al. (2018) and corrected for the perspective effect using Equation (6) of van de Ven et al. (2005) and assuming a cluster distance of 13.2 kpc (Ferraro et al. 1999, consistent with the more recent estimate by Baumgardt & Vasiliev 2021). PMs are then decomposed into projected tangential $\mu_{\rm TAN}$ and radial $\mu_{\rm RAD}$ components and converted into units of km s^{-1} using Equation (4) of van de Ven et al. (2005).

Similarly to what has been done for the line-of-sight component, we derived the velocity dispersion in both the tangential ($\sigma_{\rm TAN}$) and radial ($\sigma_{\rm RAD}$) components by dividing the sample into radial bins and using a maximum likelihood approach. The results are listed in Table 7 and shown in Figure 16 (top and middle panels). For comparison purposes, we also show the PM dispersion profile obtained by Vasiliev & Baumgardt (2021) using the Gaia EDR3 data set (blue solid line in the top panel of Figure 16). Within the errors, their results are in agreement with the profile obtained in this work (black circles), except for a couple of points at $r \sim 100''$. It is interesting to note that the radial profile of $\sigma_{\rm TAN}/\sigma_{\rm RAD}$ shown in the bottom panel of Figure 16 indicates that this cluster is characterized by an isotropic velocity distribution, although the large uncertainties do not allow us to rule out the possible presence of anisotropy. As shown in Tiongco et al. (2016), an isotropic velocity distribution would suggest that this cluster is in an advanced dynamical stage and lost any velocity anisotropy developed during its early or long-term phases of evolution (see Section 5 below for further discussion). We also derived the rotation curve in the plane of the sky by computing, again with a maximum likelihood method, the average value of $\mu_{\rm TAN}$ in each radial bin. We assumed negative $\mu_{\rm TAN}$ values in the case of a clockwise rotation in the plane of the sky (from north to west). The obtained rotation profile is shown in Figure 17 (black circles) and listed in Table 7 (last two columns). In Figure 17, the rotation curve is compared with that published in Vasiliev & Baumgardt (2021; blue solid line), showing a quite good agreement. In agreement with what was derived from line-of-sight measurements, we find a signature of clockwise rotation even in the plane of the sky, with a maximum amplitude

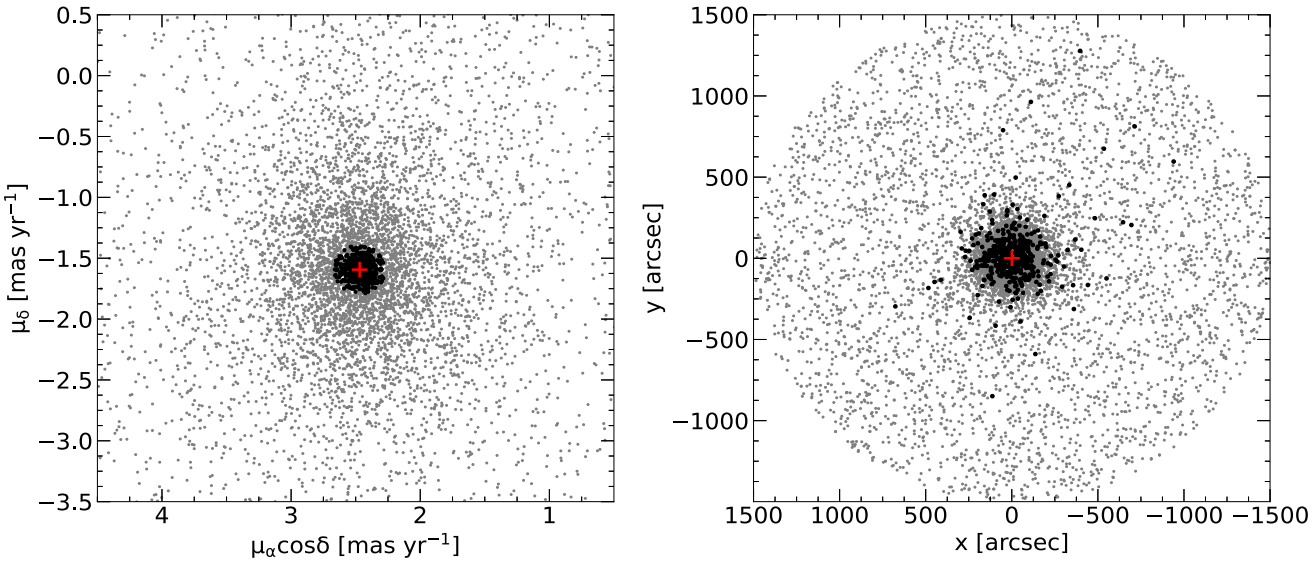

Figure 15. Left panel: VPD of the stars of the selected sample (black circles) and of the original Gaia EDR3 data set (gray points), with the red cross marking the absolute motion (Vasiliev & Baumgardt 2021). Right panel: map on the plane of the sky, with respect to the adopted cluster center (red cross), of the selected star sample (black circles) and of the original Gaia EDR3 one (gray points).

Table 7
Radial and Tangential Velocity Dispersion Profile and Rotation Curve in the Plane of the Sky of NGC 1904

r_i (arcsec)	r_e (arcsec)	N	$\sigma_{\rm RAD}$ (km s^{-1})	$\epsilon_{\sigma_{\rm RAD}}$ (km s^{-1})	$\sigma_{\rm TAN}$ (km s^{-1})	$\epsilon_{\sigma_{\rm TAN}}$ (km s^{-1})	$\mu_{\rm TAN}$ (km s^{-1})	$\epsilon_{\mu_{\rm TAN}}$ (km s^{-1})
5	45	38	5.45	0.69	5.80	0.74	0.61	1.00
45	70	65	4.25	0.54	5.00	0.57	−1.39	0.75
70	100	79	3.50	0.45	3.70	0.47	−2.04	0.62
100	150	104	4.30	0.43	3.30	0.42	−1.49	0.49
150	200	52	3.15	0.64	3.40	0.59	−1.19	0.79
200	300	59	3.10	0.56	2.70	0.59	−1.29	0.71
300	750	33	3.00	0.66	2.90	0.74	−0.29	0.84

Note. The table lists the internal and external radii of each adopted radial bin (r_i and r_e, respectively), the number of stars in each bin (N), the velocity dispersion and its uncertainty in the radial and tangential component (Columns (4)–(7)), and the average $\mu_{\rm TAN}$ and its uncertainty in each radial bin (Columns (8)–(9)).

of $\sim$−2.0 km s^{-1} at $\sim$80″ (2 projected half-mass radii or $\sim$1.5 3D half-mass radius) from the cluster center. As a final result, the rotation profile both in the plane of the sky and in the line-of-sight direction will be compared with rotation curve models with different inclination angles in Section 5.

Since for a subsample of 130 stars we have the three velocity components (i.e., RV, $\mu_\alpha \cos\delta$, and μ_δ), as a sanity check, we applied the method described in Sollima et al. (2019) to verify that the values of PA_0 and rotation amplitude estimated separately along the line of sight and the plane of the sky directions are able to properly reproduce also the 3D velocity space of the system as traced by this subsample. Following Sollima et al. (2019), in the case of rotation, a modulation of the mean velocity in the three components as a function of the angular position of the stars is detected. According to their Equation (2), for a solid-body rotation the three velocity components are

$$\begin{aligned} {\rm RV} &= \omega\, R\, \sin(\theta - {\rm PA}_0)\, \sin i \\ v_\parallel &= \omega\, R\, \sin(\theta - {\rm PA}_0)\, \cos i \\ v_\perp &= \omega\, R\, \cos(\theta - {\rm PA}_0)\, \cos i, \end{aligned} \quad (3)$$

where ω is the angular velocity, R is the projected distance from the cluster center, $0° < \theta < 360°$ is the angular position of the stars (growing anticlockwise from north to east), $0° < i < 90°$ is the inclination angle of the rotation axis with respect to the line of sight, PA_0 is the PA of the rotation axis defined as above, RV is the velocity component along the line of sight, and $v_\parallel$ and $v_\perp$ are the components in the directions parallel and perpendicular to the rotation axis, respectively (for more details see Appendix A of Sollima et al. 2019). We then defined $A = \langle \omega R \rangle$ as the average projected rotation velocity amplitude, and we assumed it negative for clockwise rotation in the plane of the sky. In our analysis, we have fixed PA_0 to the value obtained above from the line-of-sight velocities ($PA_0 = 98°$; see Section 4.3), and we then used a maximum likelihood algorithm to determine the best-fit values of i ($i = 37°$) and A ($A = -2.05$ km s^{-1}). The latter is in very good agreement with the estimates obtained from the previous analyses along the line of sight and on the plane of the sky, separately. The result of this analysis is plotted in Figure 18.

4.7. Ellipticity

A rotating system is also expected to be flattened in the direction perpendicular to the rotation axis (Chandrasekhar 1969). Although the cluster rotation measured along the line-of-sight direction has a maximum amplitude of just $\sim$1.5

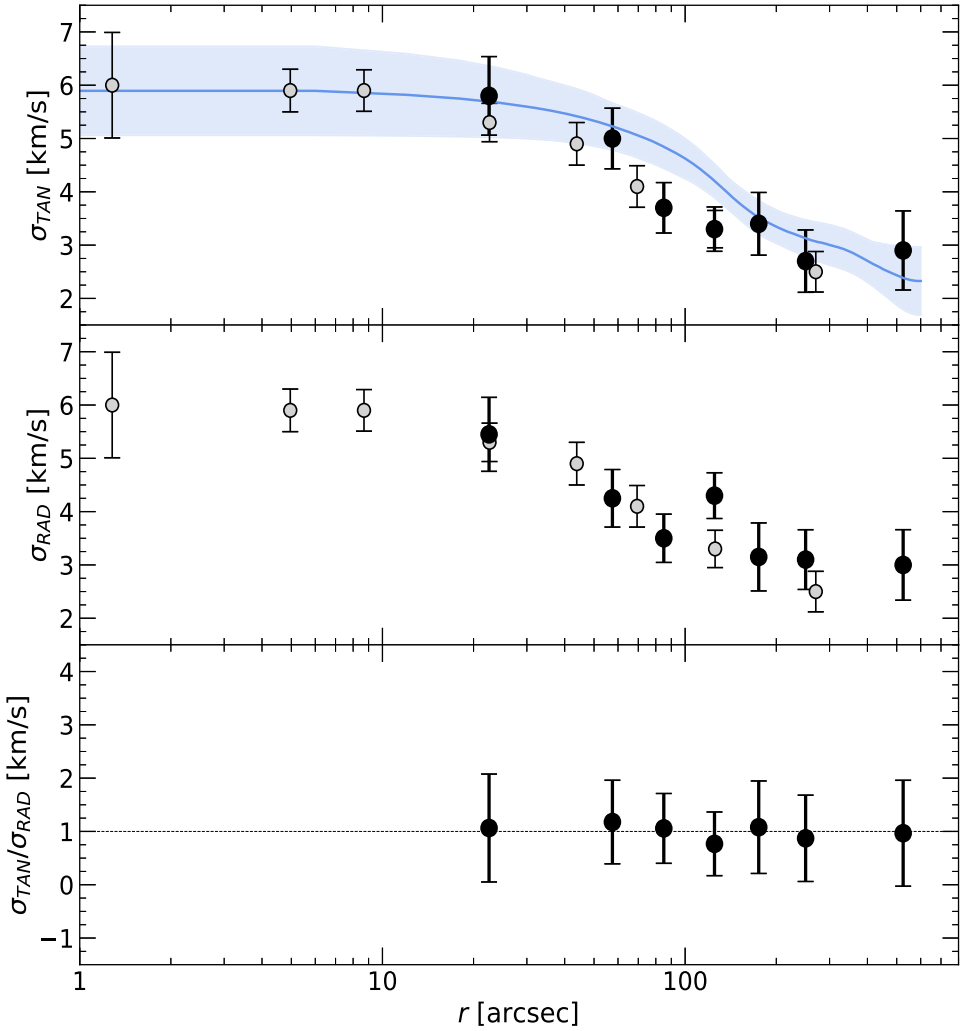

Figure 16. From top to bottom: tangential and radial velocity dispersion profiles, and anisotropy profile. The black circles mark the results obtained with the sample selected from the Gaia EDR3 data set, while the gray circles correspond to the second velocity moment profile obtained in this work from individual RVs (the same as in Figure 10). The PM dispersion profile presented in Vasiliev & Baumgardt (2021) is marked for comparison by the blue solid line in the top panel, with shaded area representing its 68% confidence interval.

km s^{-1}, we investigated the morphology of NGC 1904 by using the catalog discussed in Lanzoni et al. (2007b) to build the 2D stellar density map of the system. The analysis was limited to an area of $\sim 400'' \times 400''$, and only stars with $V < 21$ have been used to avoid incompleteness effects. The distribution of star positions was transformed into a smoothed 2D surface density function through the use of a kernel with a width of $1'$ (see Dalessandro et al. 2015). The resulting 2D density map is shown in Figure 19, where the black solid lines represent the isodensity curves, the white lines correspond to their best-fit ellipses, and the dashed line marks the position of the rotation axis estimated from the star RVs ($PA_0 = 98°$). As is clear from the figure, the stellar density distribution has spherical symmetry in the center and becomes slightly more flattened for increasing radius. The ellipticity $\epsilon = 1 - b/a$, where a and b are the major and minor axis, respectively, reaches its maximum in the external region (at $r \sim 220''$) where we measured a value of 0.04 ± 0.02, qualitatively consistent with what was found previously by Harris (1996; 0.01) and in line with the small measured rotation. Although the ellipticity is small, ellipses major axis have an orientation of $\sim 10°$ in the northeast direction, implying that the stellar density distribution is flattened in the direction perpendicular to the rotation axis in agreement with what is expected for a rotating system and qualitatively consistent with that predicted, for example, by the models introduced by Varri & Bertin (2012) and found in other observational studies (e.g., Dalessandro et al. 2021a; see also Bianchini et al. 2013; Bellini et al. 2017; Lanzoni et al. 2018a).

5. Discussion

In the context of the ongoing MIKiS survey (Ferraro et al. 2018b), in this paper we presented the velocity dispersion profile and rotation curve of the GGC NGC 1904. Thanks to a combination of different data sets acquired with appropriate spatial resolution, we measured the RV of ~1700 individual stars sampling the entire cluster radial extension.

Figure 14 shows that the velocity dispersion profile of NGC 1904 is characterized by approximately constant behavior in the innermost region and a monotonically decreasing one in the outer part. We can compare this behavior to the expectation from the King (1966) model that best fits the observed star density distribution, to verify whether it is able to simultaneously reproduce the observed structure and kinematics. In doing this, we always prefer to use the star density profile from

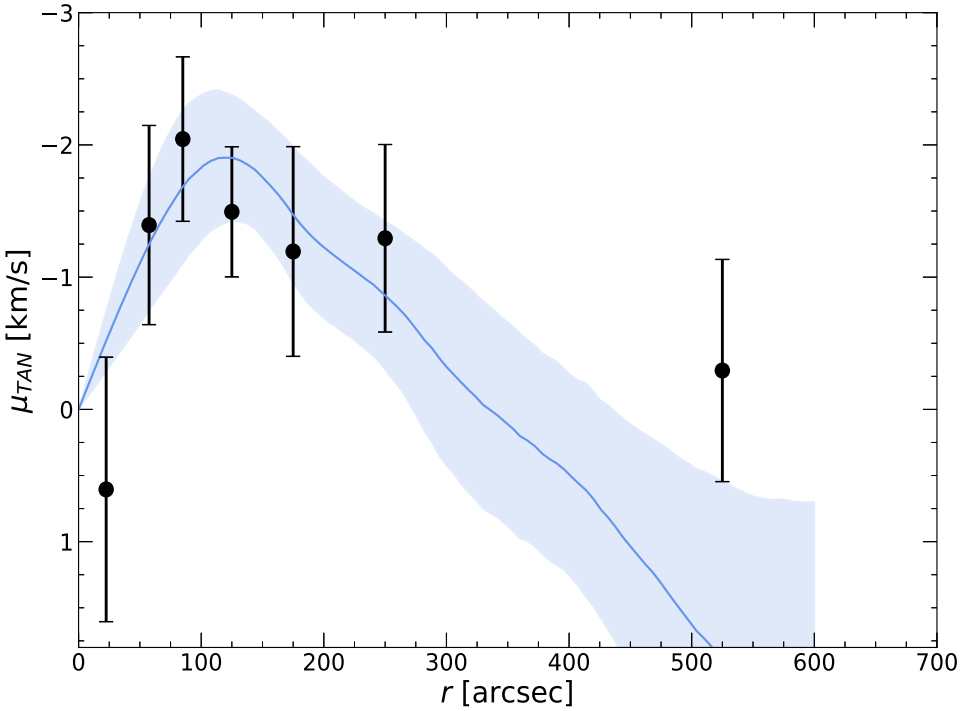

Figure 17. Rotation profile of NGC 1904 in the plane of the sky obtained with the star sample selected in this work from the Gaia EDR3 data (black circles). The solid blue line and shaded area show the PM rotation profile presented in Vasiliev & Baumgardt (2021) and its 68% confidence interval, respectively.

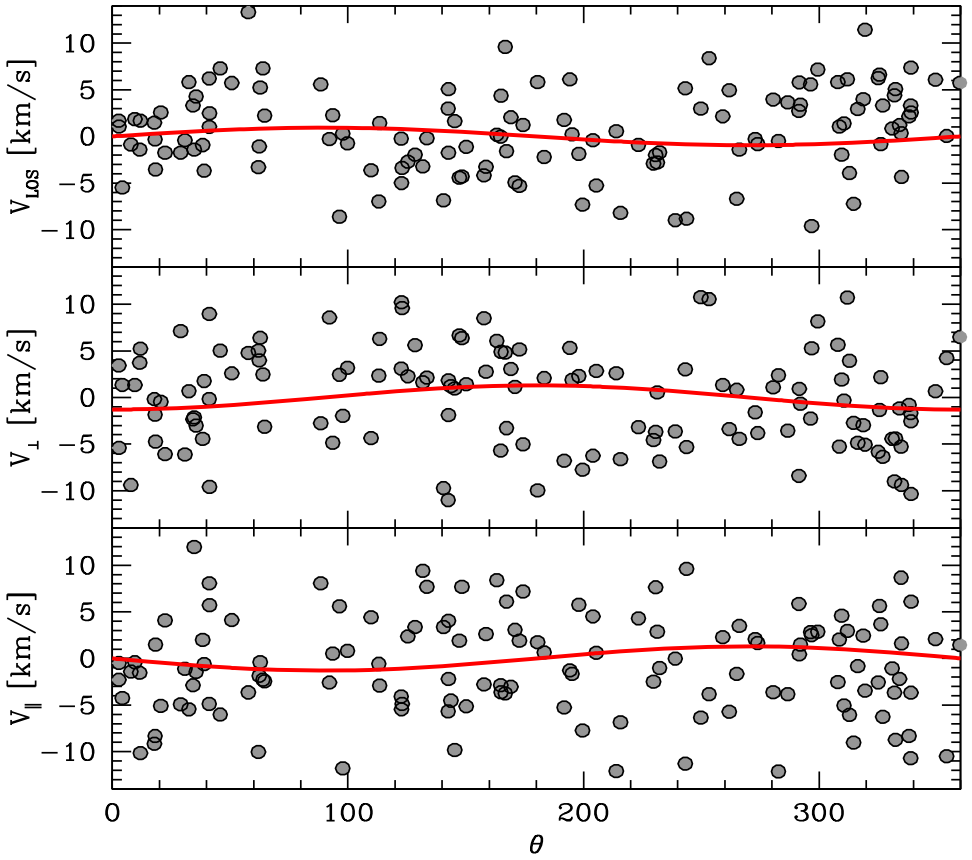

Figure 18. Distribution of the three velocity components for the 130 stars in NGC 1904, for which the 3D kinematic information is available, as a function of their angular position in degree. The red solid lines show the curves obtained for $PA_0 = 98°$ and for the best-fit values of the rotation amplitude $A = -2.05$ km s^{-1} and inclination angle $i = 37°$, as discussed in the text (see Section 4.6).

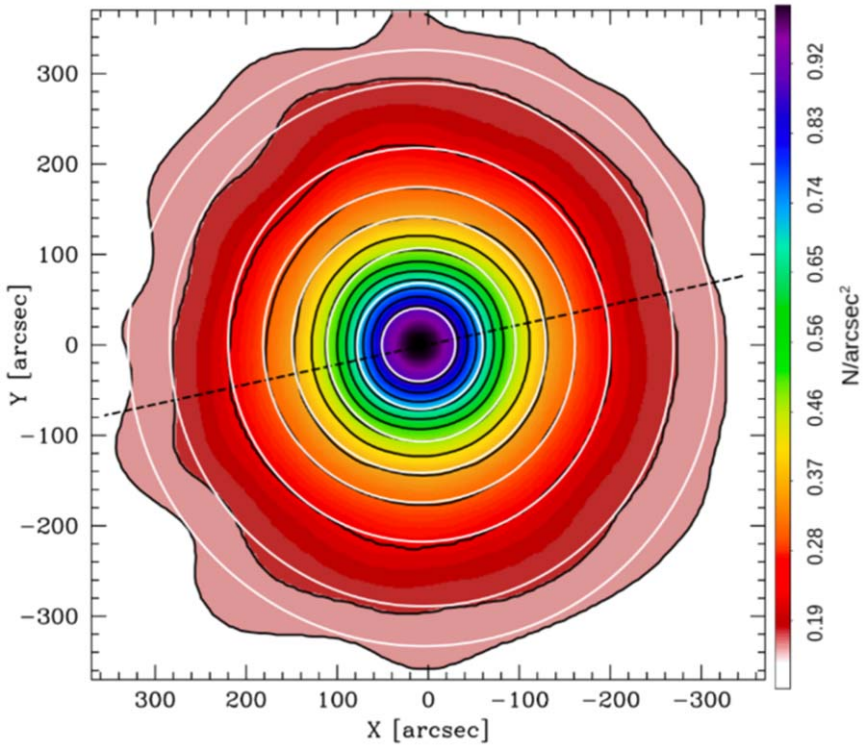

Figure 19. Smoothed stellar density map of the inner 400″ × 400″ of NGC 1904, obtained from the photometric catalog discussed in Lanzoni et al. (2007b). The solid black lines are isodensity contours, while the white curves mark their best-fit ellipses. The black dashed line marks the direction of the global rotation axis (with PA of 98°; see Section 4.4).

resolved star counts, instead of the surface brightness profile, to avoid possible biases due to the sparse presence of bright stars, which can locally alter the luminosity distribution. As discussed in Miocchi et al. (2013), the King model that best fits the star density profile of NGC 1904 is characterized by a dimensionless central potential $W_0 = 7.75$, which corresponds to a concentration parameter $c = 1.76$, defined as $c = \log(r_t/r_0)$, where $r_t = 9\farcm32$ is the cluster tidal radius and $r_0 = 9\farcm8$ is the King radius, which is similar to, although not coincident with, the core radius $r_c = 9\farcm4$. The 3D half-mass radius and the projected half-mass radius of the system are $r_h = 56\farcm7$ and $R_h = 41\farcm7$, respectively. Adopting the distance modulus quoted in Ferraro et al. (1999), which locates the cluster at a distance of ∼13.2 kpc from us, the physical sizes of the cluster structural parameters turn out to be $r_c = 0.6$ pc and $r_h = 3.63$ pc. We adopted these values as representative of the structure of the cluster, and we thus compared the projected velocity dispersion profile of this model to the observations (see Figure 14). By performing a χ^2 test, we found the value of σ_0 that minimizes the residuals between the observed velocity dispersion profile and the adopted King model. From the solutions providing $\chi^2 = \chi^2_{\rm min} \pm 1$, we then obtained the 1σ uncertainty on the best-fit value. The resulting central velocity dispersion is $\sigma_0 = 5.9 \pm 0.3$ km s^{-1}, and the comparison with the observed profile clearly shows that the adopted King model is able to nicely reproduce both the observed structure and the observed kinematics of NGC 1904. This value is in good agreement with previous determinations: it is only slightly larger than the value listed in the Harris (1996) catalog ($\sigma_0 = 5.3$ km s^{-1}) and slightly smaller than that found by Baumgardt & Hilker (2018), who quote $\sigma_0 = 6.5$ km s^{-1}, in spite of the fact that they adopt the velocity dispersion profile by Lützgendorf et al. (2013), who conversely obtain a significantly larger value of the central velocity dispersion ($\sigma_0 > 8$ km s^{-1}).

From the derived value of the central velocity dispersion we estimated the total mass of the system. To this end, we used Equation (3) in Majewski et al. (2003), where the parameters μ and β have been determined, respectively, by following Djorgovski (1993) and by assuming $\beta = 1/\sigma_0^2$ (as appropriate for models with $W_0 > 5$; see the discussion in Richstone & Tremaine 1986). The resulting total mass is $M = 1.28^{+0.15}_{-0.14} \times 10^5\, M_\odot$. The uncertainties have been estimated through a Monte Carlo simulation, performing 1000 random extractions of the values of c, r_0, and σ_0 from normal distributions centered in their best-fit values and with dispersions equal to the estimated uncertainties of the respective parameters. This mass estimate is in perfect agreement with the value obtained in Ferraro et al. (2018b; $1.29 \times 10^5\, M_\odot$) and slightly smaller than the values quoted in McLaughlin & van der Marel (2005; $1.58^{+0.15}_{-0.14} \times 10^5\, M_\odot$), Lützgendorf et al. (2013; $(1.44 \pm 0.10) \times 10^5\ M_\odot$), and Baumgardt & Hilker (2018; $(1.69 \pm 0.11) \times 10^5\ M_\odot$). These differences can be justified taking into account all the uncertainties and the fact that the estimates have been obtained through different methods.

A signature of systemic rotation in the outskirts of this cluster ($85'' < r < 200''$), with a maximum amplitude of 1.7 km s^{-1} and a PA of 108° for the rotation axis, was already presented in Ferraro et al. (2018b). Here we unambiguously confirm the presence of global rotation in the line-of-sight component using complementary data that sample the innermost regions. A well-defined rotation pattern with a rotation axis PA of 98° has been found. The resulting rotation curve is presented in Figure 13 and is well described by the analytical

Table 8
Summary of the Parameters Used and the Main Results Obtained in This Work for the GGC NGC 1904

Parameter	Estimated Value	Reference
Cluster center (deg)	R.A. = 81.0462112	Lanzoni et al. (2007b)
	Decl. = −24.5247211	
Color excess	$E(B-V) = 0.01$	Ferraro et al. (1999)
Metallicity	[Fe/H] = −1.6	Harris (1996)
Cluster distance	$d = 13.2$ kpc	Ferraro et al. (1999)
3D half-mass radius	$r_h = 56.7^{+0}_{-0.005}$	Miocchi et al. (2013)
2D projected half-mass radius	$R_h = 41.68^{+0.08}_{-0.03}$	Miocchi et al. (2013)
Dimensionless central potential	$W_0 = 7.75^{+0.05}_{-0.1}$	Miocchi et al. (2013)
Concentration parameter	$c = 1.76^{+0.02}_{-0.03}$	Miocchi et al. (2013)
Core radius	$r_c = 9.4^{+0.6}_{-0.3}$	Miocchi et al. (2013)
Tidal radius	$r_t = 9.32^{+0.04}_{-0.09}$	Miocchi et al. (2013)
Systemic velocity	$V_{sys} = 205.4 \pm 0.2$ km s^{-1}	this work
Central velocity dispersion	$\sigma_0 = 5.9 \pm 0.3$ km s^{-1}	this work
Line-of-sight rotation peak	$A_{peak} = 1.5$ km s^{-1}	this work
Plane-of-the-sky rotation peak	$A = -2.0$km s^{-1}	this work
Rotation axis PA	PA = 98°	this work
Inclination angle of the rotation axis	$i = 37°$	this work
Absolute proper motions	$\mu_\alpha \cos\delta = 2.469 \pm 0.025$ mas yr^{-1}	Vasiliev & Baumgardt (2021)
	$\mu_\delta = -1.594 \pm 0.025$ mas yr^{-1}	
Ellipticity	$\epsilon = 0.04 \pm 0.02$	this work
Total mass	$M = 1.28^{+0.15}_{-0.14} \times 10^5 M_\odot$	this work

Note. All radii are in units of arcseconds, with the exception of r_t, which is in arcminutes.

expression introduced in Lynden-Bell (1967) to describe the equilibrium rotational profile emerging at the end of violent relaxation. The peak of the rotation curve ($A_{peak} \sim 1.5$ km s^{-1}) is located at a distance from the cluster center of about 1.5 3D half-mass radius (or nearly 2 projected half-mass radii). To obtain the full characterization of the internal kinematics of the cluster, we analyzed the stellar PMs from the Gaia EDR3 data, detecting a signal of rotation also in the plane of the sky (see Figure 17). To double-check these results, we then applied the procedure described in Sollima et al. (2019) to the subsample of 130 stars for which we have the three velocity components (RVs and PMs). By fixing the rotation axis PA to the value obtained from the measured RVs ($PA_0 = 98°$), this analysis confirmed the presence of a rotation pattern with the previously determined amplitude, and it provided us with an estimate of the inclination angle of the rotation axis with respect to the line of sight: $i = 37°$. The main final results are summarized in Table 8, which also lists all the parameters of the cluster used in this work.

Theoretical studies (e.g., Fiestas et al. 2006; Ernst et al. 2007; Hong et al. 2013; Tiongco et al. 2017) have shown that star clusters gradually lose their initial rotation as a result of the effects of internal two-body relaxation and angular momentum loss carried away by escaping stars. Hence, the extent of the present-day rotation detected in many GGCs (see, e.g., Bianchini et al. 2013; Fabricius et al. 2014; Bellini et al. 2017; Ferraro et al. 2018b; Kamann et al. 2018b; Lanzoni et al. 2018a; Sollima et al. 2019; Dalessandro et al. 2021a) represents only a lower limit to the primordial rotation of these systems and suggests that the initial cluster kinematics might be characterized by a stronger rotation (Hénault-Brunet et al. 2012; Mackey et al. 2012; Kamann et al. 2018a; Dalessandro et al. 2021b). To address this issue for the case of NGC 1904, in Figure 20 we compare the observed rotation (black squares) with the results (colored lines) of a representative *N*-body simulation of a rotating star cluster from the survey of models presented in Tiongco et al. (2016). The results reported here are those from the VBrotF04 model (see Tiongco et al. 2016 for further details), a system initially set up with phase-space properties following those of the rotating models introduced by Varri & Bertin (2012). We emphasize that a study specifically aimed at identifying the best evolutionary model for NGC 1904 would require an extensive investigation following the evolution of systems with a broad range of different initial conditions. The purpose of our comparison here is just to illustrate a general dynamical path leading to the observed rotational properties of NGC 1904. Figure 20 shows the rotation curves in the plane of the sky (top panels) and in the line-of-sight direction (bottom panels). From left to right, the inclination angle of the simulated cluster rotation axis with respect to the line-of-sight direction varies from $i = 30°$, to $i = 40°$, to $i = 50°$ (see labels), which are values close to that determined by the analysis presented in Section 4.6 ($i = 37°$). Curves of different colors correspond to simulated rotation curves obtained at different evolutionary times, as labeled in the top left panel. The comparison with the observations shows a general good agreement, both on the plane of the sky and along the line-of-sight direction, with the rotation curves obtained in advanced evolutionary phases of the *N*-body model, when the system has lost a significant fraction of its initial angular momentum. Hence, the cluster rotational properties suggest an old dynamical age for NGC 1904, in agreement with what is inferred from the radial distribution of blue straggler stars (see Ferraro et al. 2012, 2018b, 2020; Lanzoni et al. 2016). This study shows the importance of a complete 3D kinematic characterization of stellar systems. Indeed, it not only allows a proper determination of the actual strength of the cluster internal rotation but also allows us to constrain the dynamical phase of the system. The synergy between measurements of the structural and kinematic properties, as in the case of NGC 1904, can provide the essential

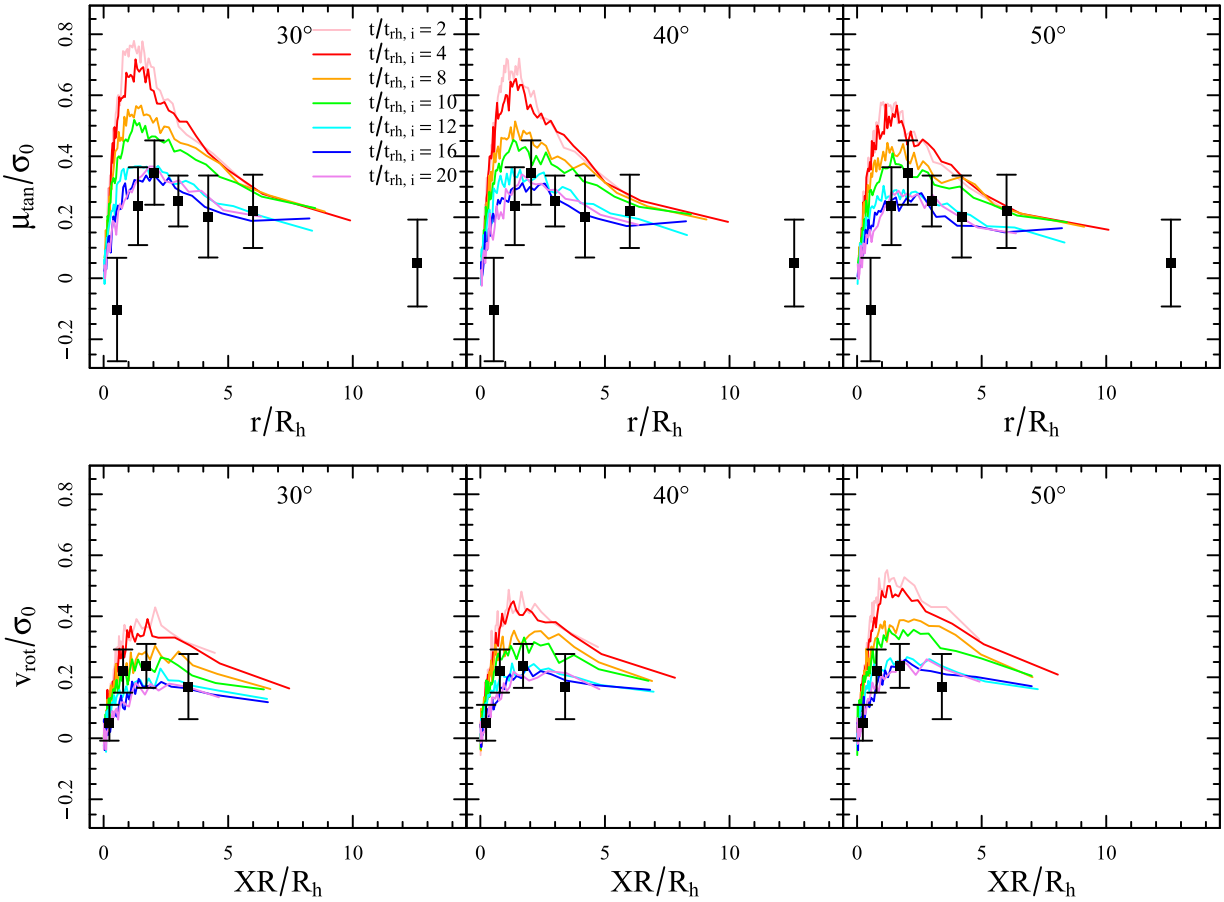

Figure 20. Comparison between the observed rotation curves normalized to the central velocity dispersion (black squares) and the results from the *N*-body simulations of Tiongco et al. (2016, VBrotF04 model, see their Table 1), obtained at different evolutionary times (curves of different colors; see labels in the top left panel, where $t_{hr,i}$ is the cluster's initial half-mass relaxation time). The top and bottom panels show, respectively, the rotation in the plane of the sky and that in the line-of-sight direction. From left to right, the results obtained for different inclination angles between the line of sight and the rotation axis of the simulated cluster are shown: $i = 30°$, $i = 40°$, $i = 50°$, as labeled. The distance from the cluster center (top panel) and the distance from the rotation axis (bottom panel) are normalized to the projected half-mass radius (R_h).

ingredients necessary to build a complete picture of the formation and dynamical history of GGCs.

This work is part of the project Cosmic-Lab at the Physics and Astronomy Department "A. Righi" of the Bologna University (http://www.cosmic-lab.eu/ Cosmic-Lab/Home.html). The research was funded by the MIUR throughout the PRIN-2017 grant awarded to the project Light-on-Dark (PI:Ferraro) through contract PRIN-2017K7REXT. A.L.V. acknowledges support from a UKRI Future Leaders Fellowship (MR/S018859/1).

ORCID iDs

Silvia Leanza https://orcid.org/0000-0001-9545-5291
Cristina Pallanca https://orcid.org/0000-0002-7104-2107
Francesco R. Ferraro https://orcid.org/0000-0002-2165-8528
Barbara Lanzoni https://orcid.org/0000-0001-5613-4938
Emanuele Dalessandro https://orcid.org/0000-0003-4237-4601
Livia Origlia https://orcid.org/0000-0002-6040-5849
Alessio Mucciarelli https://orcid.org/0000-0001-9158-8580
Elena Valenti https://orcid.org/0000-0002-6092-7145
Anna Lisa Varri https://orcid.org/0000-0002-6162-1594
Enrico Vesperini https://orcid.org/0000-0003-2742-6872

References

Bacon, R., Accardo, M., Adjali, L., et al. 2010, Proc. SPIE, 7735, 131
Bailyn, C. D. 1995, ARA&A, 33, 133
Baumgardt, H., & Hilker, M. 2018, MNRAS, 478, 1520
Baumgardt, H., & Vasiliev, E. 2021, MNRAS, 505, 5957
Bellazzini, M., Dalessandro, E., Sollima, A., & Ibata, R. 2012, MNRAS, 423, 844
Bellini, A., Bianchini, P., Varri, A. L., et al. 2017, ApJ, 844, 167
Bianchini, P., Varri, A. L., Bertin, G., & Zocchi, A. 2013, ApJ, 772, 67
Cadelano, M., Chen, J., Pallanca, C., et al. 2020, ApJ, 905, 63
Cadelano, M., Pallanca, C., Ferraro, F. R., et al. 2017, ApJ, 844, 53
Cadelano, M., Ransom, S. M., Freire, P. C. C., et al. 2018, ApJ, 855, 125
Chandrasekhar, S. 1969, ApJ, 157, 1419
Dalessandro, E., Miocchi, P., Carraro, G., Jílková, L., & Moitinho, A. 2015, MNRAS, 449, 1811
Dalessandro, E., Raso, S., Kamann, S., et al. 2021a, MNRAS, 506, 813
Dalessandro, E., Salaris, M., Ferraro, F. R., Mucciarelli, A., & Cassisi, S. 2013, MNRAS, 430, 459
Dalessandro, E., Varri, A. L., Tiongco, M., et al. 2021b, ApJ, 909, 90
Djorgovski, S. 1993, in ASP Conf. Ser. 50, Structure and Dynamics of Globular Clusters, ed. S. G. Djorgovski & G. Meylan (San Francisco, CA: ASP), 373
D'Orazi, V., Gratton, R. G., Angelou, G. C., et al. 2015, MNRAS, 449, 4038
Ernst, A., Glaschke, P., Fiestas, J., Just, A., & Spurzem, R. 2007, MNRAS, 377, 465
Fabricius, C., Luri, X., Arenou, F., et al. 2021, A&A, 649, A5
Fabricius, M. H., Noyola, E., Rukdee, S., et al. 2014, ApJL, 787, L26
Ferraro, F. R., Beccari, G., Dalessandro, E., et al. 2009, Natur, 462, 1028
Ferraro, F. R., Clementini, G., Fusi Pecci, F., Sortino, R., & Buonanno, R. 1992, MNRAS, 256, 391

Ferraro, F. R., D'Amico, N., Possenti, A., Mignani, R. P., & Paltrinieri, B. 2001, ApJ, 561, 337
Ferraro, F. R., Lanzoni, B., & Dalessandro, E. 2020, Rendiconti Lincei. Scienze Fisiche e Naturali, 31, 19
Ferraro, F. R., Lanzoni, B., Dalessandro, E., et al. 2012, Natur, 492, 393
Ferraro, F. R., Lanzoni, B., Dalessandro, E., et al. 2019, NatAs, 3, 1149
Ferraro, F. R., Lanzoni, B., Raso, S., et al. 2018a, ApJ, 860, 36
Ferraro, F. R., Lapenna, E., Mucciarelli, A., et al. 2016, ApJ, 816, 70
Ferraro, F. R., Messineo, M., Fusi Pecci, F., et al. 1999, AJ, 118, 1738
Ferraro, F. R., Mucciarelli, A., Lanzoni, B., et al. 2018b, ApJ, 860, 50
Ferraro, F. R., Mucciarelli, A., Lanzoni, B., et al. 2018c, Msngr, 172, 18
Ferraro, F. R., Pallanca, C., Lanzoni, B., et al. 2015, ApJL, 807, L1
Ferraro, F. R., Paltrinieri, B., Fusi Pecci, F., et al. 1997, A&A, 324, 915
Ferraro, F. R., Sills, A., Rood, R. T., Paltrinieri, B., & Buonanno, R. 2003, ApJ, 588, 464
Fiestas, J., Spurzem, R., & Kim, E. 2006, MNRAS, 373, 677
Forbes, D. A., & Bridges, T. 2010, MNRAS, 404, 1203
Freitag, M., Guerkan, M. A., & Rasio, F. A. 2007, ASP Conf. Ser. 367, Massive Stars in Interactive Binaries, ed. N. St. Louis & A. F. J. Moffat, (San Francisco, CA: ASP), 707, arXiv:astro-ph/0410327
Gaia Collaboration, Brown, A. G. A., Vallenari, A., et al. 2021, A&A, 649, A1
Gaia Collaboration, Helmi, A., van Leeuwen, F., et al. 2018, A&A, 616, A12
Giersz, M., Leigh, N., Hypki, A., Lützgendorf, N., & Askar, A. 2015, MNRAS, 454, 3150
Harris, W. E. 1996, AJ, 112, 1487, 2010 edition
Hénault-Brunet, V., Gieles, M., Evans, C. J., et al. 2012, A&A, 545, L1
Hong, J., Kim, E., Lee, H. M., & Spurzem, R. 2013, MNRAS, 430, 2960
Kacharov, N., Bianchini, P., Koch, A., et al. 2014, A&A, 567, A69
Kamann, S., Bastian, N., Husser, T.-O., et al. 2018a, MNRAS, 480, 1689
Kamann, S., Husser, T. O., Brinchmann, J., et al. 2016, A&A, 588, A149
Kamann, S., Husser, T. O., Dreizler, S., et al. 2018b, MNRAS, 473, 5591
King, I. R. 1966, AJ, 71, 64
Kurucz, R. L. 2005, MSAIS, 8, 14
Lanzoni, B., Dalessandro, E., Ferraro, F. R., et al. 2007a, ApJL, 668, L139
Lanzoni, B., Ferraro, F. R., Alessandrini, E., et al. 2016, ApJL, 833, L29
Lanzoni, B., Ferraro, F. R., Dalessandro, E., et al. 2010, ApJ, 717, 653
Lanzoni, B., Ferraro, F. R., Dalessandro, E., et al. 2019, ApJ, 887, 176
Lanzoni, B., Ferraro, F. R., Mucciarelli, A., et al. 2018a, ApJ, 861, 16
Lanzoni, B., Ferraro, F. R., Mucciarelli, A., et al. 2018b, ApJ, 865, 11
Lanzoni, B., Mucciarelli, A., Origlia, L., et al. 2013, ApJ, 769, 107
Lanzoni, B., Sanna, N., Ferraro, F. R., et al. 2007b, ApJ, 663, 1040
Lindegren, L., Klioner, S. A., Hernández, J., et al. 2021, A&A, 649, A2
Lützgendorf, N., Kissler-Patig, M., Gebhardt, K., et al. 2013, A&A, 552, A49
Lynden-Bell, D. 1967, MNRAS, 136, 101
Mackey, A. D., Costa, G. S. D., Ferguson, A. M. N., & Yong, D. 2012, ApJ, 762, 65
Magorrian, J., Tremaine, S., Richstone, D., et al. 1998, AJ, 115, 2285
Majewski, S. R., Skrutskie, M. F., Weinberg, M. D., & Ostheimer, J. C. 2003, ApJ, 599, 1082
Mapelli, M., Colpi, M., Possenti, A., & Sigurdsson, S. 2005, MNRAS, 364, 1315
Martin, N. F., Ibata, R. A., Chapman, S. C., Irwin, M., & Lewis, G. F. 2007, MNRAS, 380, 281
McLaughlin, D. E., & van der Marel, R. P. 2005, ApJS, 161, 304
Miocchi, P., Lanzoni, B., Ferraro, F. R., et al. 2013, ApJ, 774, 151
Pallanca, C., Beccari, G., Ferraro, F. R., et al. 2017, ApJ, 845, 4
Pallanca, C., Dalessandro, E., Ferraro, F. R., Lanzoni, B., & Beccari, G. 2013, ApJ, 773, 122
Pallanca, C., Dalessandro, E., Ferraro, F. R., et al. 2010, ApJ, 725, 1165
Pallanca, C., Lanzoni, B., Ferraro, F. R., et al. 2021, ApJ, 913, 137
Pallanca, C., Ransom, S. M., Ferraro, F. R., et al. 2014, ApJ, 795, 29
Pooley, D., Lewin, W. H. G., Anderson, S. F., et al. 2003, ApJL, 591, L131
Portegies Zwart, S. F., Baumgardt, H., Hut, P., Makino, J., & McMillan, S. L. W. 2004, Natur, 428, 724
Pryor, C., & Meylan, G. 1993, in ASP Conf. Ser. 50, Structure and Dynamics of Globular Clusters, ed. S. G. Djorgovski & G. Meylan (San Francisco, CA: ASP), 357
Ransom, S. M., Hessels, J. W. T., Stairs, I. H., et al. 2005, Sci, 307, 892
Raso, S., Libralato, M., Bellini, A., et al. 2020, ApJ, 895, 15
Richstone, D. O., & Tremaine, S. 1986, AJ, 92, 72
Riello, M., De Angeli, F., Evans, D. W., et al. 2021, A&A, 649, A3
Sbordone, L., Bonifacio, P., Castelli, F., & Kurucz, R. L. 2004, ATLAS and SYNTHE under Linux, arXiv:astro-ph/0406268
Scarpa, R., Marconi, G., Carraro, G., Falomo, R., & Villanova, S. 2011, A&A, 525, A148
Sollima, A., Baumgardt, H., & Hilker, M. 2019, MNRAS, 485, 1460
Sollima, A., Bellazzini, M., Smart, R. L., et al. 2009, MNRAS, 396, 2183
Stetson, P. B. 1987, PASP, 99, 191
Stetson, P. B., Pancino, E., Zocchi, A., Sanna, N., & Monelli, M. 2019, MNRAS, 485, 3042
Tiongco, M. A., Vesperini, E., & Varri, A. L. 2016, MNRAS, 455, 3693
Tiongco, M. A., Vesperini, E., & Varri, A. L. 2017, MNRAS, 469, 683
Tonry, J., & Davis, M. 1979, AJ, 84, 1511
Usher, C., Kamann, S., Gieles, M., et al. 2021, MNRAS, 503, 1680
van de Ven, G., van den Bosch, R. C. E., Verolme, E. K., & de Zeeuw, P. T. 2005, Astro & Astrophysics, 445, 513
van den Bosch, R., de Zeeuw, T., Gebhardt, K., Noyola, E., & van de Ven, G. 2006, ApJ, 641, 852
Varri, A. L., & Bertin, G. 2012, A&A, 540, A94
Vasiliev, E., & Baumgardt, H. 2021, MNRAS, 505, 5978
Walker, M. G., Mateo, M., Olszewski, E. W., et al. 2006, AJ, 131, 2114
Weilbacher, P. M., Palsa, R., Streicher, O., et al. 2020, A&A, 641, A28